Anisotropic ray-Born migration/inversion: A synthetic modeling study

David W.S. Eaton and Robert R. Stewart

ABSTRACT

A least-squares migration/inversion technique is used to investigate the resolution of isotropic and anisotropic parameters for a transversely isotropic earth model. The method is based on the elastic ray-Born approximation, which linearizes the forward modeling problem using far-field, high-frequency and small-perturbation assumptions. Approximate background ray-Green's tensors comprise the kernel of the scattering integral, and are computed using a finite-difference approach. Least-squares inversion is implemented using an iterative three-step conditioned-gradient procedure. The first step for each iteration resembles prestack Kirchhoff depth migration of the current data residual, yielding a gradient subimage for each model parameter. An approximate Hessian operator is then applied to partially deconvolve parameter-coupling effects, producing a set of model-perturbation images. Finally, a predicted forward model is computed by scattering from the current set of model perturbations. This scheme attempts to recover short-wavelength parameter variations relative to the reference model, rather than its slowly varying components.

The resolution of P- and S-wave velocities, density and Thomsen's anisotropy parameters is investigated for the case of a homogeneous, isotropic background model, using both surface and crosswell acquisition geometries. A third example, involving an anticline structure, composed of anisotropic, inhomogeneous layers is used to demonstrate the feasibility of these techniques for seismic imaging in structurally complex areas. Finally, a ray-traced (non-Born) dataset illustrates that superior resolution of subsurface features (in particular, slope discontinuities) can be achieved by migrating all elastic wave types simultaneously.

INTRODUCTION

Seismic migration and inversion are closely related processes for obtaining images of the subsurface. Underlying principles and methodologies vary, but in essence both techniques attempt to quantify the task of inferring physical and structural parameters from seismic data. Historically, the term inversion has been applied to the problem of estimating intrinsic properties that characterize a physical system (Tarantola, 1987), whereas the term migration has been reserved for imaging of the structural configuration of geologic discontinuities (Stolt and Benson, 1986). In both cases, however, the mathematical link between observed data and the final image is the same: a set of equations of motion that are derived from a constitutive

model for the earth.

When a constitutive model is chosen such that properties of the earth at any point are independent of direction, the model is said to be isotropic. Conversely, virtually all of the constituent minerals in the earth's crust have crystal structures that are anisotropic (Musgrave, 1970). Anisotropy on a macroscopic scale can be caused by preferred orientation of anisotropic minerals, as well as periodic thin layering and stress aligned fracturing (Crampin et al., 1984). Fundamental differences exist between wave prop-agation in an anisotropic versus an isotropic solid (Duff, 1960; Crampin, 1981). Previous studies of seimic imaging in anisotropic media (Meadows, 1985; Geoltrain and Cohen, 1989; Uren et al., 1990; Tura, 1990) have stressed the importance of accounting for anisotropic wave propagation effects, but have dealt primarily with special cases, such as elliptical anisotropy or plane layering.

This study deals with migration and inversion of seismic data in the presence of transverse isotropy, a widely applicable form of anisotropy. The methodology used here is a synthesis of ray, Born and generalized least-squares inverse theory. The geophysical literature contains numerous examples of similar ray-Born imaging techniques applied to seismic data, predicated upon various assumptions about the nature of the background medium. In order of increasing complexity (and ill-posedness of the inverse problem), these assumptions range from constant-density acoustic media (eg. Cohen and Bleistein, 1979; Beylkin, 1985; Miller et al., 1987) and variable-density acoustic media (eg. Raz, 1981; Clayton and Stolt, 1981; Weglein et al., 1986; Lebras and Clayton, 1988) to isotropic-elastic media (Beydoun and Mendes, 1989; Beydoun et al., 1989, 1990; Beylkin and Burridge, 1990) and fractured media (Tura, 1990). The methodology employed here is based primarily on an elastic ray-Born migration/inversion technique introduced by Beydoun and Mendes (1989). However, Beydoun and Mendes (1989) considered 2-D isotropic-elastic media, whereas here the medium is assumed to be 2-1/2 dimensional and transversely isotropic.

Implicit in the ray approximation used here are the assumptions that near-field effects can be neglected, and that the scale length of parameter variations for the background medium are large compared to the dominant seismic wavelength. Our migration/inversion technique makes use of the following additional assumptions:

1) The anisotropic symmetry system is transversely isotropic. The direction of the symmetry axis can vary, but must lie in the plane of acquisition.

2) The medium is two dimensional, with mirror symmetry across the plane of acquisition (ie. shooting across geologic strike). This assumption allows the use of 2-dimensional modeling with 2-1/2 dimensional corrections, instead of full 3-dimensional modeling.

3) Using *a priori* information, it is possible to define elastic parameters for a reference medium that are smoothly varying and a close approximation to the true earth parameters. This assumption is required to validate the Born approximation.

4) Preprocessing of the data has removed coherent energy caused by surface waves, multiples, etc., that are not accounted for in the modeling procedure.

The aim of this study is to present several new techniques for both forward modeling and inversion for a transversely isotropic medium. We will start with a

description of the finite-difference algorithm used to calculate the background Green's tensors. The method described here is an extension of finite-difference techniques introduced by Vidale (1988) and Vidale and Houston (1990) for isotropic media. This approach is particularly well suited to imaging problems because all quantities are computed directly on a regular grid; thus no subsequent interpolation is required. Next the algorithm for forward and inverse scattering will be reviewed. Most of the accompanying theory is covered by Eaton (1990), Eaton and Stewart (1990) and Eaton (1991), and is therefore omitted here. Several examples are then presented, to highlight the advantages and limitations of this approach.

FINITE-DIFFERENCE TRAVELTIME CALCULATION

A practical requirement for this migration/inversion method is the ability to compute high-frequency (ray) Green's functions corresponding to a relatively general class of inhomogeneous, transversely isotropic elastic media. Specifically, at each point in the model space, the traveltime, particle-motion vector, initial slowness, out-of-plane spreading factor (τ_{22}) and geometrical spreading function must be known. This information is required for all wave types and source/receiver locations. Collectively, these quantities are referred to here as the ray-Green's parameters. Experience has shown that calculation of these parameters constitutes a major comp-utational bottleneck, particularly for an inhomogeneous, anisotropic reference model. For brevity, only the traveltime and amplitude calculations will be reviewed here. A discussion of how the other ray-Green's parameters are obtained can be found in Eaton (1991).

In an inhomogeneous, anisotropic elastic medium, the high-frequency travel-time function, τ, is governed by the eikonal equation (Cerveny, 1972; Gajewski and Psencik, 1987; Kendall and Thompson, 1989)

$$\det[c_{ijkl}p_jp_l - \rho\delta_{ik}] = 0 \quad , \tag{1}$$

where $c_{ijkl}(\mathbf{x})$ is the elastic stiffness tensor, and $p_j(\mathbf{x}) \equiv \partial\tau/\partial x_j = \tau_{,j}$ defines the slowness vector and ρ is density. Typically, the eikonal equation is solved along characteristics, or rays. Here, an approximate solution to equation (1) under the initial condition $\tau = 0$ at $\mathbf{x} = \mathbf{x_s}$ is sought using a technique similar to the method proposed by Vidale (1988) and modified by Qin et al. (1990). However, a hexagonal mesh of points is employed here (see Fig. 1), similar to grids used in fluid-flow modeling studies involving cellular automata (eg. Rothman, 1988). This choice of grids reduces grid-anisotropy effects (Eaton, 1990).

For the general three-dimensional, anisotropic case, solving the eikonal equation requires the solution of a sixth-order polynomial. In essence, the strategy is to use estimates of two components of the slowness vector, $\mathbf{p}$, to deduce the value of the third component. The problem is simplified for 2-1/2 dimensional propagation in the plane of symmetry, since p_2 (the component of slowness normal to the symmetry plane) vanishes. Suppose that for a given four-point stencil the traveltime is known at points A, B and D (Figure 1). The stencil defines a local co-ordinate system, with the x_3-axis pointing from A-C. Because this direction may not coincide with the
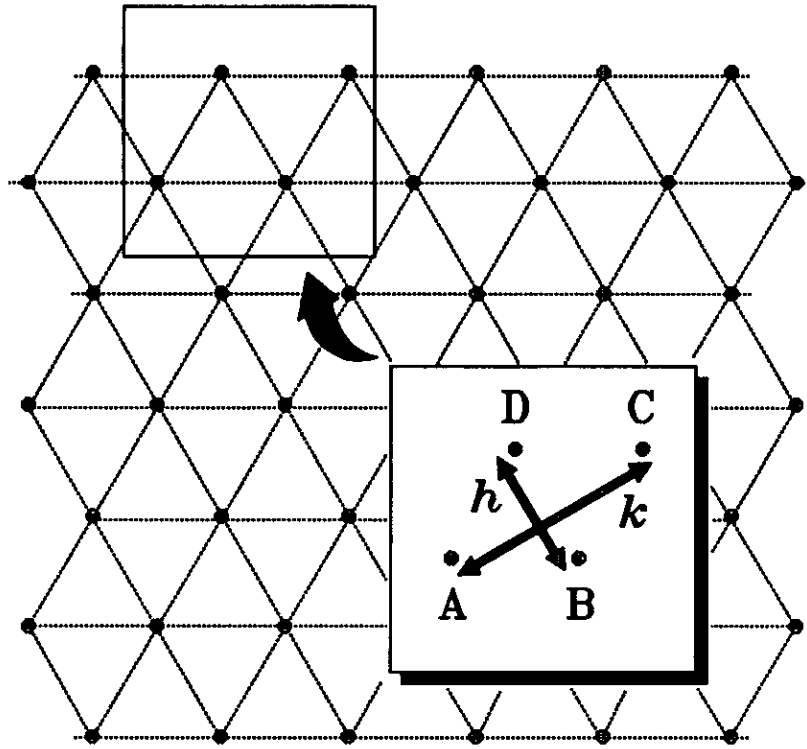
FIG. 1. Hexagonal mesh used for finite-difference calculations. Inset: Example of a four-point finite-difference stencil.

anisotropic symmetry axis, it is generally necessary to rotate the stiffness tensor into the correct orientation. Using the approximation

$$p_1 \approx \frac{\tau_D - \tau_B}{h} \quad , \tag{2}$$

the traveltime at point C is given by

$$\tau_C = \tau_A + p_3 k \quad , \tag{3}$$

where p_3 is chosen to satisfy the eikonal equation (1) at the centre of the stencil. Since p_1 and p_2 are both known, the eikonal equation may be rewritten as the sixth-order polynomial

$$\xi_j p_3^{\ j} = 0 \quad , \ j = 0, \dots, 6 \quad . \tag{4}$$

the coefficients of which are given in Appendix A.

In this study, an iterative technique is used to solve $f(p_3)$. First, the direction of propagation with respect to the local axis of symmetry is estimated. Using this, along with known the wave type (ie. qP, qSV or SH), an initial guess of the phase velocity can be obtained, which in turn can be used to give an estimate of p_3, knowing p_1. Starting with this initial guess, Newton's method is employed to refine the solution. For most cases, this approach converges rapidly (approximately 1-8 iterations, depending on the degree of anisotropy). The algorithm has the most difficulty near a shear-wave singularity because of the highly nonlinear nature of $f(p_3)$.

Following Vidale (1988), the initial step in the overall procedure is to time the points in the immediate vicinity of the source point (the source is given a traveltime of zero). For the type of grid considered here, there are six grid nodes neighbouring the source (Figure 2), forming a hexagon. The traveltime to each point is simply

$$\tau = \Delta x / v \quad , \tag{5}$$

where Δx is the distance between each node on the grid and v is the group velocity given by

$$v_i = \frac{c_{ijkl} p_l D_{jk}}{\rho D_{qq}} \quad , \tag{6}$$

where D_{jk} is a cofactor of the matrix $[c_{ijkl} p_i p_l - \rho \delta_{jk}]$ (Kendall and Thompson, 1989). This set of six points comprises the initial computational front. After each subsequent iteration, the new computational front is taken to be the set of points that have been timed, but are not completely surrounded by time point (circles in Figure 2). This set of points will roughly approximate the true wavefront at each iteration. The algorithm proceeds by determining the node that has the minimum traveltime on the computational front. The traveltime to all nodes bordering the minimum are then computed by solving equation (4) as described above. By rigourously working away from traveltime minima, this method honours the principle of causality, even in the presence of large parameter contrasts (Qin et al., 1990). The procedure is repeated until all points on the grid within some prespecified zone of interest have been timed.

AMPLITUDE CALCULATION

In the zeroth-order ray approximation, seismic amplitudes are governed by the transport equation (Cerveny, 1972),

$$2A_{,i}^0 v_i + \rho^{-1} A^0 (\rho v_i)_{,i} = 0 \quad . \tag{7}$$

A function $A^0(\mathbf{x})$ that satisfies the transport equation is often referred to as a geometrical-spreading function. If the amplitude is known at one point along a ray, the amplitude can be extrapolated using the relation (Cerveny, 1972; Cerveny et al., 1977)
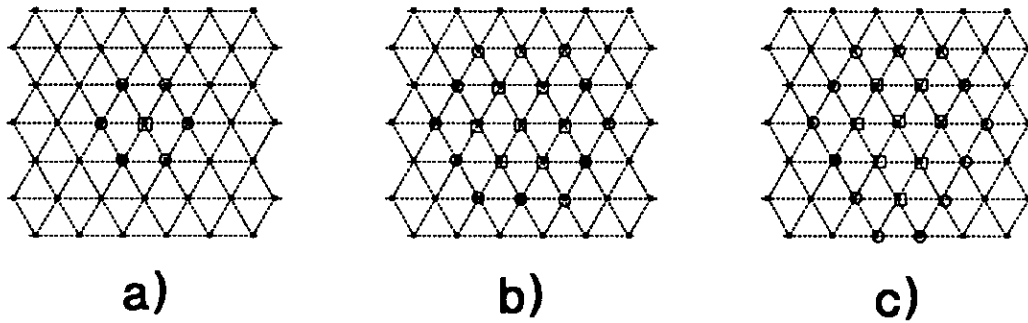
FIG. 2. a) The first step in the algorithm is the calculation of times for the six neighbouring points around source point (square). The current wavefront is represented by circles. The solid circle indicates the point with the minimum τ on the current wavefront. b) Timed points after several more iterations. Squares represent points that are timed, but not on the current wavefront. c) Timed points one iteration after b).

$$\frac{A_2}{A_1} = \left[\frac{\rho_1 V_1 J_1}{\rho_2 V_2 J_2}\right] \quad , \tag{8}$$

where $V(x)$ is the local phase velocity and the quantity J is known as the *ray Jacobian*, and can be defined as follows. Let us denote parameters specifying the initial conditions at the start of a ray (eg. longitudinal and radial takeoff angles) as γ_1 and γ_2. Tracing three rays from the source with initial parameters (γ_1, γ_2), $(\gamma_1 + \delta\gamma_1, \gamma_2)$ and $(\gamma_1, \gamma_2 + \delta\gamma_2)$ will define a *ray tube* (Figure 3). J is related to a differential surface element on a wavefront bounded by the ray tube via the relation (Gajewski and Psencik, 1987)

$$\delta\sigma = J\delta\gamma_1\delta\gamma_2 \quad . \tag{9}$$

Expansion or contraction of the ray tube corresponds to a geometrical amplitude decrease or increase, repectively. Surfaces along which the ray Jacobian vanishes are known as caustics (Aki and Richards, 1980).

Vidale and Houston (1990) suggested a finite-difference technique for amplitude calculation based on these geometrical concepts, rather than direct solution of the transport equation. Here, their method is extended to include anisotropic media. The first step is to calculate the initial takeoff angle at the source. This is accomplished by computing the traveltime from four grid nodes surrounding the source location (Figure 4). The initial slowness on the ray from S^0 to P is then given by
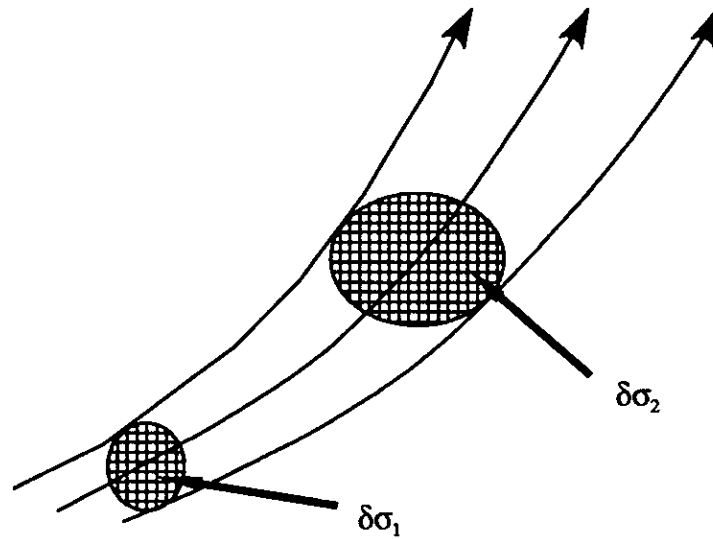
FIG. 3. Differential surface elements $\delta\sigma_1$ and $\delta\sigma_2$ contained within a ray tube.

$$p_1^0 = \frac{-\tau_1 - \tau_2 + \tau_3 + \tau_4}{2\Delta x}$$

$$p_3^0 = \frac{-\tau_1 + \tau_2 + \tau_3 - \tau_4}{2\sqrt{3}\,\Delta x}$$

(10)

where τ_j is the traveltime from S_j to P, and Δx is the spacing between grid points. Once the components of slowness are known, the initial phase angle can be computed using

$$\theta^0 = \tan^{-1}(p_1^0/p_3^0) \quad .$$

(11)

Estimation of the geometrical-spreading function rests on the assumption that the length of intersection of the wavefront at a point P with the circular region containing the six points surrounding P (Figure 5) is constant (roughly equal to $2\Delta x$). The accuracy of this assumption depends on the in-plane radius of curvature of the wavefront, which should be large. The change in the first ray parameter, θ^0, corresponding to this arc length, ds, is approximated by
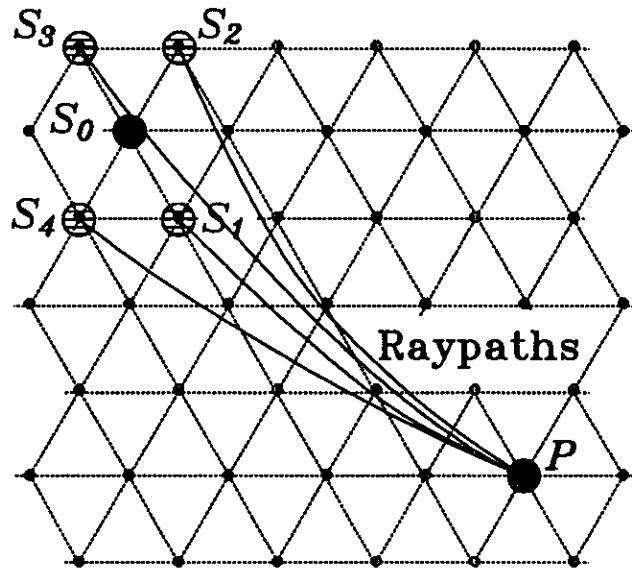
FIG. 4. Sketch of the raypaths joining four closely spaced source points (S_1, S_2, S_3 and S_4) to a point P on the grid (modified from Vidale and Houston, 1990). Differentiating the traveltimes computed from the four neighbouring source points yields the initial slowness for the ray from S_0 to P.
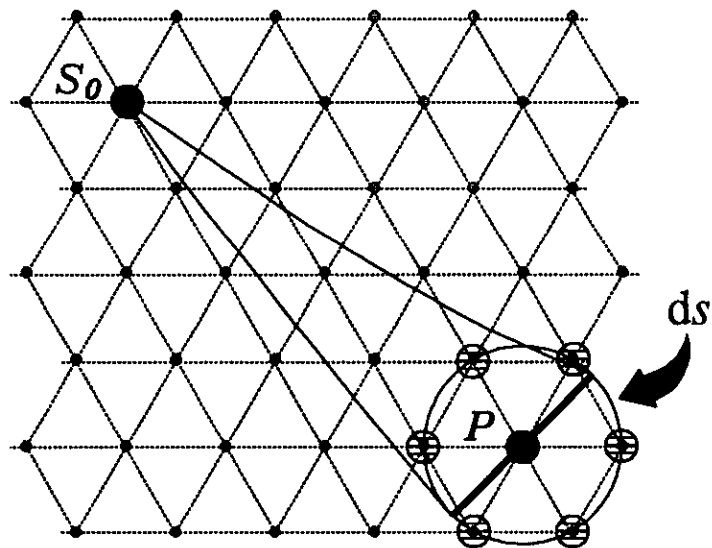
FIG. 5. Method for calculating $\Delta\gamma_1$. The total change in the initial phase angle corresponding to the line element ds on the wavefront is approximated by the difference $\theta^0_{max} - \theta^0_{min}$ for the six points neighbouring P.

$$\Delta\gamma_1 = \Delta\theta^0 - \theta_{max} - \theta_{min} \quad , \tag{12}$$

where θ_{max} and θ_{min} are the maximum and minimum initial phase angle from the set of six points surrounding P. Since ds is taken to be constant, the total area of the far-field surface element, $d\sigma$, is then proportional to the quantity $y(\theta^0,\tau)$. The corresponding near-field surface element, $d\sigma_0$, belonging to the respective ray tube can be estimated numerically for some arbitrary small traveltime, given θ^0, $\Delta\gamma_1$, $p_2(\theta^0)$ and knowledge of the geometry of the wavefront in the homogeneous region near the source. The amplitude function is then computed using the formula

$$\hat{A} = \left[\frac{\rho_0 V_0 d\sigma_0}{\rho V d\sigma}\right]^{1/2} A_0(\mathbf{p}^0) \quad , \tag{13}$$

The initial amplitude, A^0, is computed using an asymptotic form of the Green's function for a homogeneous, anisotropic medium (see Eaton, 1991).

The amplitude function obtained in this manner usually contains artifacts due to the approximations made here, and small errors in the quantities computed from previous steps. As a general rule, a mild low-pass filter is applied to remove some of these artifacts. Another general limitation of this treatment of seismic amplitudes is the use of geometrical spreading only; amplitude variations related to reflection/ transmission at interfaces, attenuation, etc., are not accounted for.

EXAMPLE TRAVELTIME AND AMPLITUDE CALCULATION

We will consider an example that illustrates the ability of this technique to model wave propagation in a complex medium. This model (see Figures 6 and 7) incorporates an anticline structure, and contains both isotropic and anisotropic layers. In addition, several of the layers in this model have elastic properties (as well as orientation of the symmetry axis) that vary continuously with position. The computed seismic traveltimes for qP waves are shown in Figure 8, and the corresponding amplitudes are shown in Figure 9. The amplitude function, in particular, shows several interesting features. Note the likely presence of two caustics for this model, indicated by the linear high-amplitude features. The modeling of these amplitude anomalies without any undue instability is a desirable feature of this approach, compared to more conventional amplitude calculation by ray tracing.

THE RAY-BORN APPROXIMATION

The ray-Born approximation for elastic media (Beylkin and Burridge, 1990) combines approximate ray-Green's tensors with the first Born approximation. This formalism comprises the basis for elastic modeling and inversion in this study. The precise form of the relation depends on the choice of parameterization. Only one set
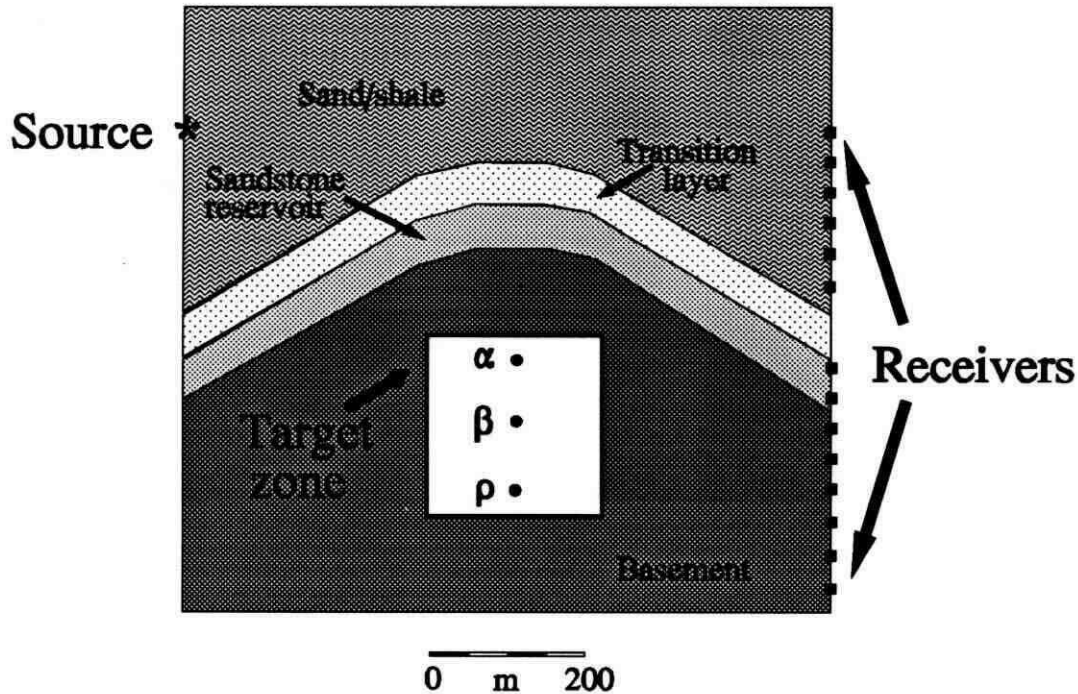
FIG. 6. Layer configuration for model 3. The first layer is a TI composite material consisting of thin sand and shale layers in equal proportion (Levin, 1979). The anisotropic symmetry axis is normal to the layer boundary. The second and third layers are partially anisotropic, but with a symmetry axis parallel to the layer boundary (to represent fracturing). Both layers are nearly isotropic at the sides of the model, but become progressively more anisotropic toward the core of the anticline. In addition, the transition layer is isotropic at the top, with a gradual increase in anisotropy toward the base of the unit. The underlying basement unit is isotropic, but with a linear velocity gradient normal to the layer boundary. The area shown is 1275 m across and 1000 m deep. Smoothed elastic parameters used for the calculation of Green's functions are displayed in Figure 7. Crosswell shooting geometry and target-zone parameters are discussed in the text.

FIG. 7. (next page) Gray scale plots of the medium parameters for model 3.

α

2750   (m/s)   5250

β

1250   (m/s)   2750

ρ

1250   (kg/m³)   2700

γ

0   0.3

δ

-0.1   0

ε

0   0.08
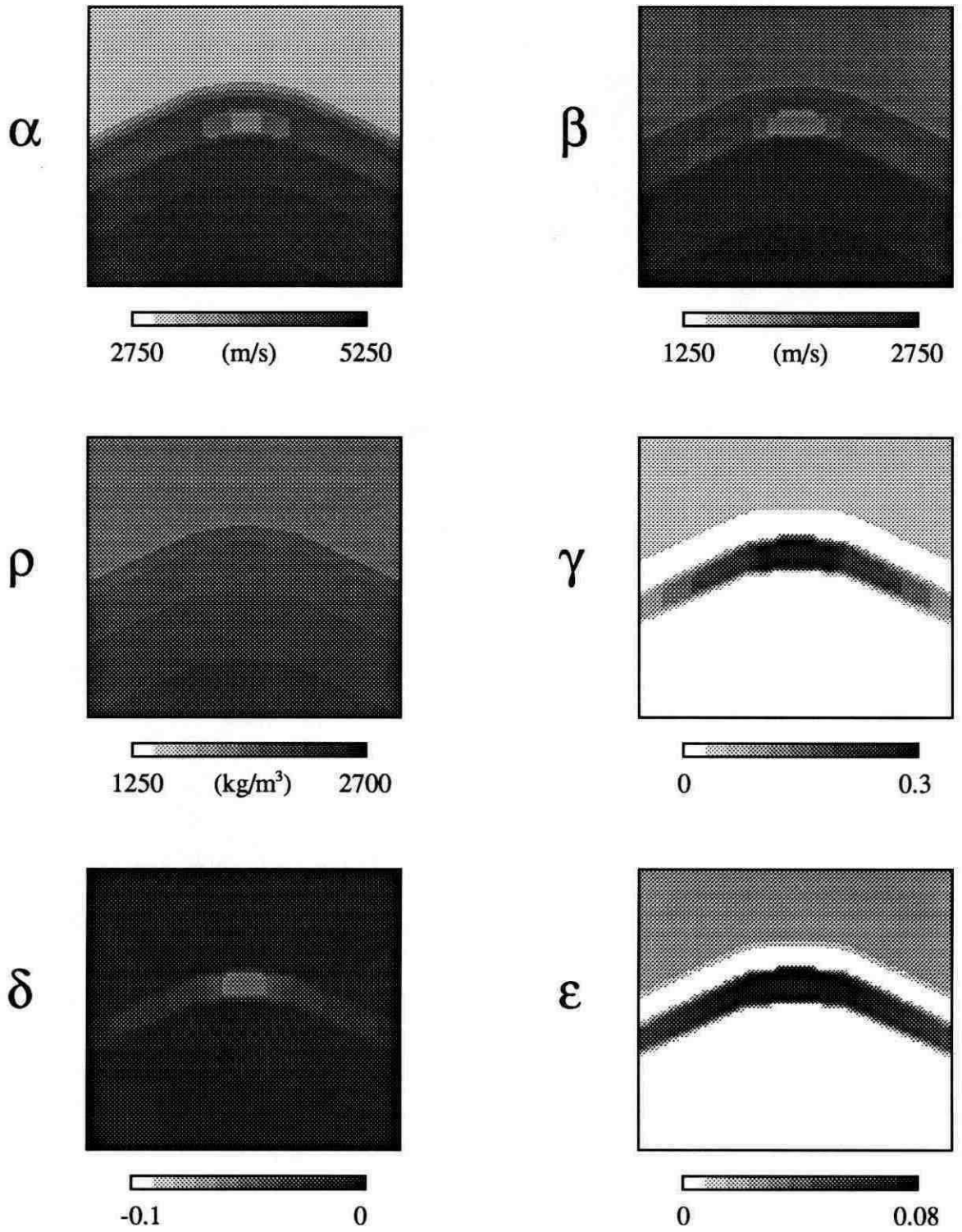
FIG. 7
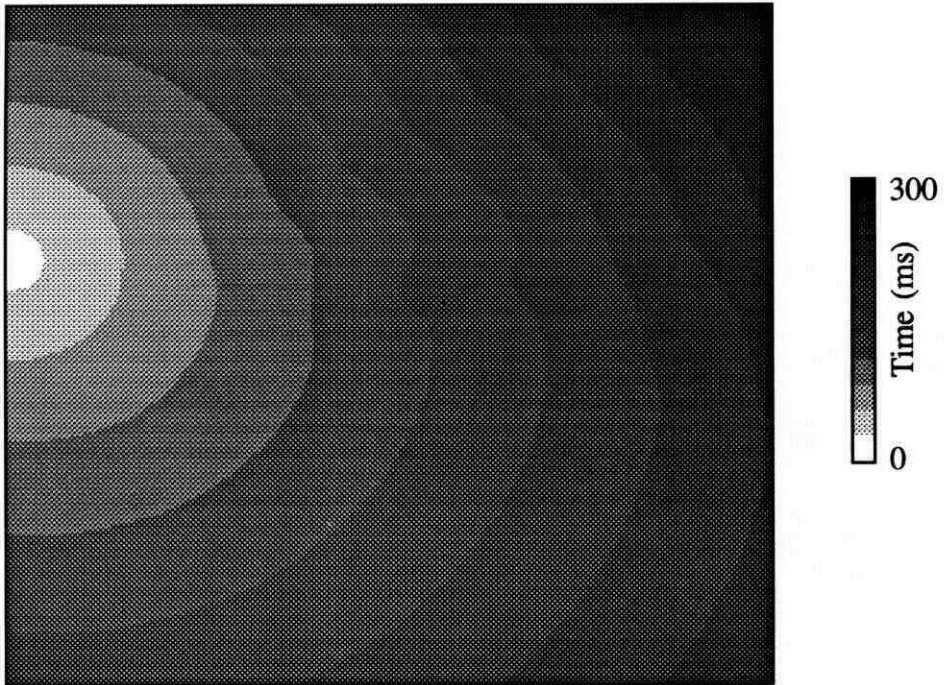
FIG. 8. Finite-difference qP traveltimes for model 3.
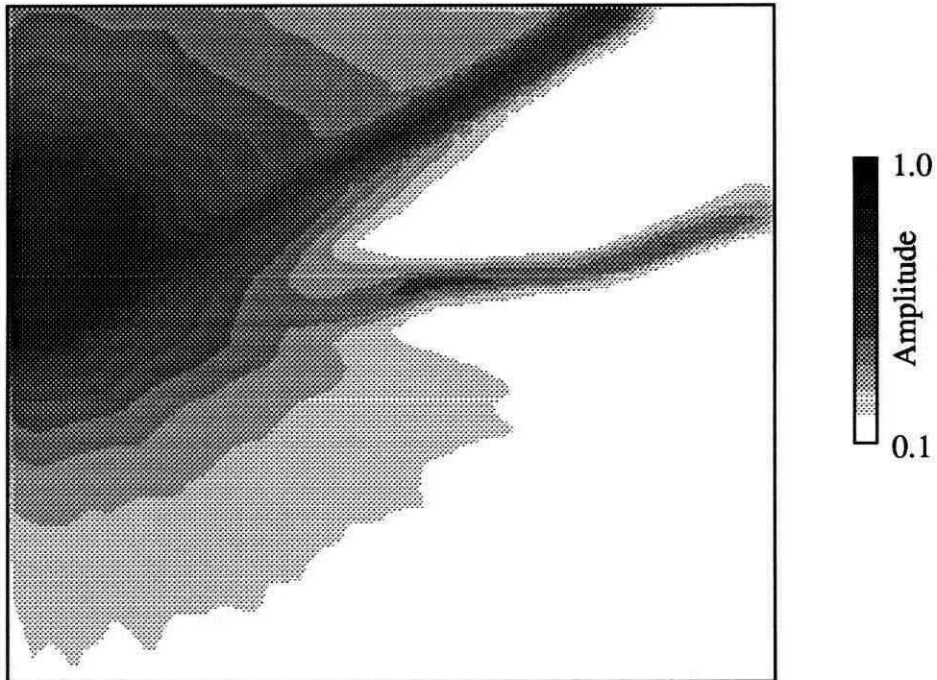
FIG. 9. Normalized geometrical-spreading amplitude function for qP waves (model 3).

of parameters has been tested here, consisting of the P- and S-wave velocity in the direction of the symmetry axis, Thomsen's (1986) anisotropy parameters and density. Defined in terms of the elastic stiffnesses, the first five parameters may be written (Thomsen, 1986)

$$\alpha_0 \equiv (C_{33}\rho^{-1})^{1/2} \quad ,$$

$$\beta_0 \equiv (C_{44}\rho^{-1})^{1/2} \quad ,$$

$$\gamma \equiv \frac{C_{66}-C_{44}}{2C_{44}} \quad , \tag{14}$$

$$\delta \equiv \frac{(C_{13}+C_{44})^2 - (C_{33}-C_{44})^2}{2C_{33}(C_{33}-C_{44})} \quad ,$$

and

$$\varepsilon \equiv \frac{C_{11}-C_{33}}{2C_{33}} \quad .$$

The dimensionless parameters γ, δ and ε have been chosen in a physically meaningful way. In the limit of weak anisotropy, ε and γ represent the factor normally associated with qP- and SH-wave anisotropy (ie. the fractional difference between the fast and slow velocities). The remaining factor, δ, governs the behaviour of qP and qSV wavefields for propagation directions close to the symmetry axis.

Details of the derivation of the ray-Born scattering formula for the particular assumptions employed here are given in Eaton and Stewart (1990). The final expression may be written

$$U_{mn}(x,y,t) \approx S'(t) * \sum_{\Omega} \tilde{g}_m(s)\hat{g}_n(r) \sum_{i,j} [s_p L_{pq} \Delta m_q^{(i,j)}](\tau_{,22})^{-1/2} A\delta(t-\tau) \quad . \tag{15}$$

Using the superscripts ~ and ^ to denote quantities associated with the source and receiver Green's tensor, the terms A, τ and $\tau_{,22}$ in equation (15) are given by

$$A(x,x_s,x_r) = \tilde{A}(x,x_s)\cdot\hat{A}(x,x_r)$$

$$\tau(x,x_s,x_r) = \tilde{\tau}(x,x_s)+\hat{\tau}(x,x_r) \quad , \tag{16}$$

$$\tau_{,22}(x,x_s,x_r) = \tilde{\tau}_{,22}(x,x_s)+\hat{\tau}_{,22}(x,x_r)$$

where x_s and x_r are the locations of the source and receiver. The vector $\Delta m^{(i,j)}$ represents the model parameter perturbations at the $(i,j)th$ pixel, and is transformed to stiffnesses by L (see Appendix B). s controls the elastic radiation patterns for individual scattering points, and is given by

$$s = (\ \hat{p}_1\hat{p}_1\hat{g}_1\hat{g}_1, \ \hat{p}_3\hat{p}_3\hat{g}_3\hat{g}_3, \ \hat{p}_1\hat{p}_3\hat{g}_1\hat{g}_3 + \hat{p}_3\hat{p}_1\hat{g}_3\hat{g}_1, \ \hat{p}_1\hat{p}_1\hat{g}_3\hat{g}_3 + \hat{p}_3\hat{p}_3\hat{g}_1\hat{g}_1 +$$

$$\hat{p}_1\hat{p}_3\hat{g}_3\hat{g}_1 + \hat{p}_3\hat{p}_1\hat{g}_1\hat{g}_3, \ 0, \ -\hat{g}_q\hat{g}_q)^T \quad , \tag{17}$$

for qP and qSV waves, and

$$s = (0, \ 0, \ 0, \ \hat{p}_3\hat{p}_3, \ \hat{p}_1\hat{p}_1, \ -1)^T \quad , \tag{18}$$

for SH waves, where **p** is a slowness vector and **g** is a unit particle-motion vector (see Crampin, 1981) associated with the respective Green's tensors. These formulae apply also to the isotropic case, but can be simplified since **g** is always either parallel or perpendicular to **p** (see Beylkin and Burridge, 1990). Finally, $S'(t)$ is the source wavelet, after filtering by the operator $\omega^{3/2}e^{i\pi/4}$, and the summation index Ω denotes the set of elastic wave types { qP, qSV, SH }.

The ray-Born scattering operator may be rewritten as

$$\Delta u = B\Delta m \quad , \tag{19}$$

to emphasize the linear relationship between data and model parameters implied by equation (15).

LEAST-SQUARES MIGRATION/INVERSION

The large dimensions of **B** (typically $10^5 \times 10^4$ or larger) preclude the use of standard matrix methods to invert for Δm. Instead, a generalized least-squares approach is adopted here, allowing us to handle noise as well as insufficient and innaccurate data in a meaningful way. We begin by defining the objective function

$$E = \frac{1}{2}(\Delta u \ {}^*W_u\Delta u + \Delta m \ {}^*W_m\Delta m) \quad , \tag{20}$$

where W_u^{-1} and W_m^{-1} are *a priori* covariance operators associated with the data and model, respectively. The strategy is to determine a model for the earth such that E is minimized. Assuming that the initial model is a close approximation to the actual earth, minimization is accomplished by requiring that the gradient function, $g \equiv \nabla E$, goes to zero. Using equation (20), we can write the gradient function as

$$g = -B \ {}^*W_u\Delta u + W_m\Delta m \quad . \tag{21}$$

The W_u operator represents a weighting function applied to the data residual to favour or suppress certain components of the data, according to available *a priori* information or criteria such as SNR or semblance (eg. Milkereit, 1987). In the absence of any such information, W_u is simply an identity matrix. The B^* operator (the conjugate transpose of **B**) maps each sample in the filtered data-residual vector to the corresponding path

of constant traveltime in the model space. Thus, $\mathbf{B}^*$ can be thought of as a filtered backprojection operator, and is very similar to prestack Kirchhoff migration in its implementation. The last term in equation (21) prevents the solution from diverging too far from the initial model ($\Delta\mathbf{m} = 0$), and thus has the role of a damping term. The absence of any such *a priori* constraints on the model is expressed mathetmatically by $\mathbf{W}_m = 0$. In this case the solution is undamped, but is also generally ill-posed (Tarantola, 1987).

Following Beydoun and Mendes (1989), we use an approximate Hessian operator to condition the gradient estimate given by equation (21). In the Gauss-Newton approximation (Adby and Dempster, 1974), the Hessian ($\mathbf{H} \equiv \nabla\mathbf{g}$) is given by

$$\mathbf{H} = \mathbf{B}^*\mathbf{W}_u\mathbf{B} + \mathbf{W}_m \quad . \tag{22}$$

The (even more) approximate Hessian operator suggested by Beydoun and Mendes (1989) makes the further assumption that $\mathbf{H}$ is diagonal, and thus does not account for interaction between neighbouring points in the model, but does acount for interaction between different parameters for the same point. This assumption is similar to the single-scatter assumption implicit in the Born approximation, and leads to a small (up to 6×6) matrix for each model pixel, that can be inverted analytically.

The model update for each iteration may be written

$$\Delta\mathbf{m} = \lambda\hat{\mathbf{H}}^{-1}\mathbf{g} \quad . \tag{23}$$

The parameter λ determines the step size, and is given by

$$\lambda = \frac{\displaystyle\sum_d \sum_t \Delta u(t)\Delta u_{sc}(t)}{\displaystyle\sum_d \sum_t (\Delta u_{sc}(t))^2} \quad , \tag{24}$$

where the sum over d represents the sum over all of the data traces, and

$$\mathbf{u}_{sc} = \mathbf{B}\hat{\mathbf{H}}^{-1}\mathbf{g} \quad . \tag{25}$$

Additional details concerning the migration/inversion algorithm can be found in Eaton (1991).

ELASTIC-MIGRATION IMPULSE RESPONSE

Valuable insight into the nature of the elastic migration aspect of the procedure can be gained by studying its impulse response. Figures 10-13 show plots of the impulse response function for various source and receiver orientations. A single trace containing a band-limited zero-phase pulse at a time of 500 ms was used to generate
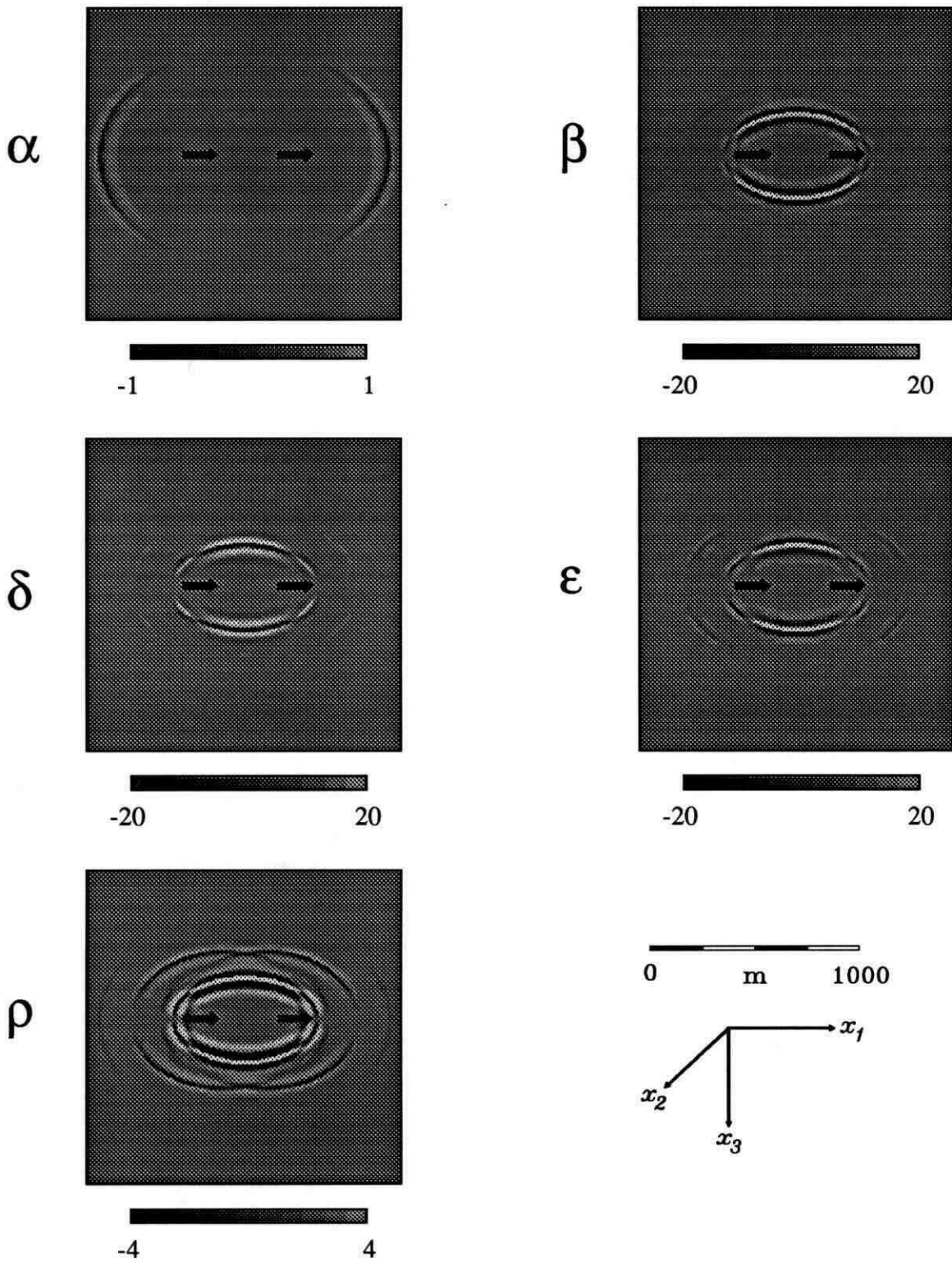
FIG. 10. Impulse response of migration operator, for source (rightmost arrow) and receiver (leftmost arrow) in the x_1-direction. Scale bars indicate relative plot amplitude.
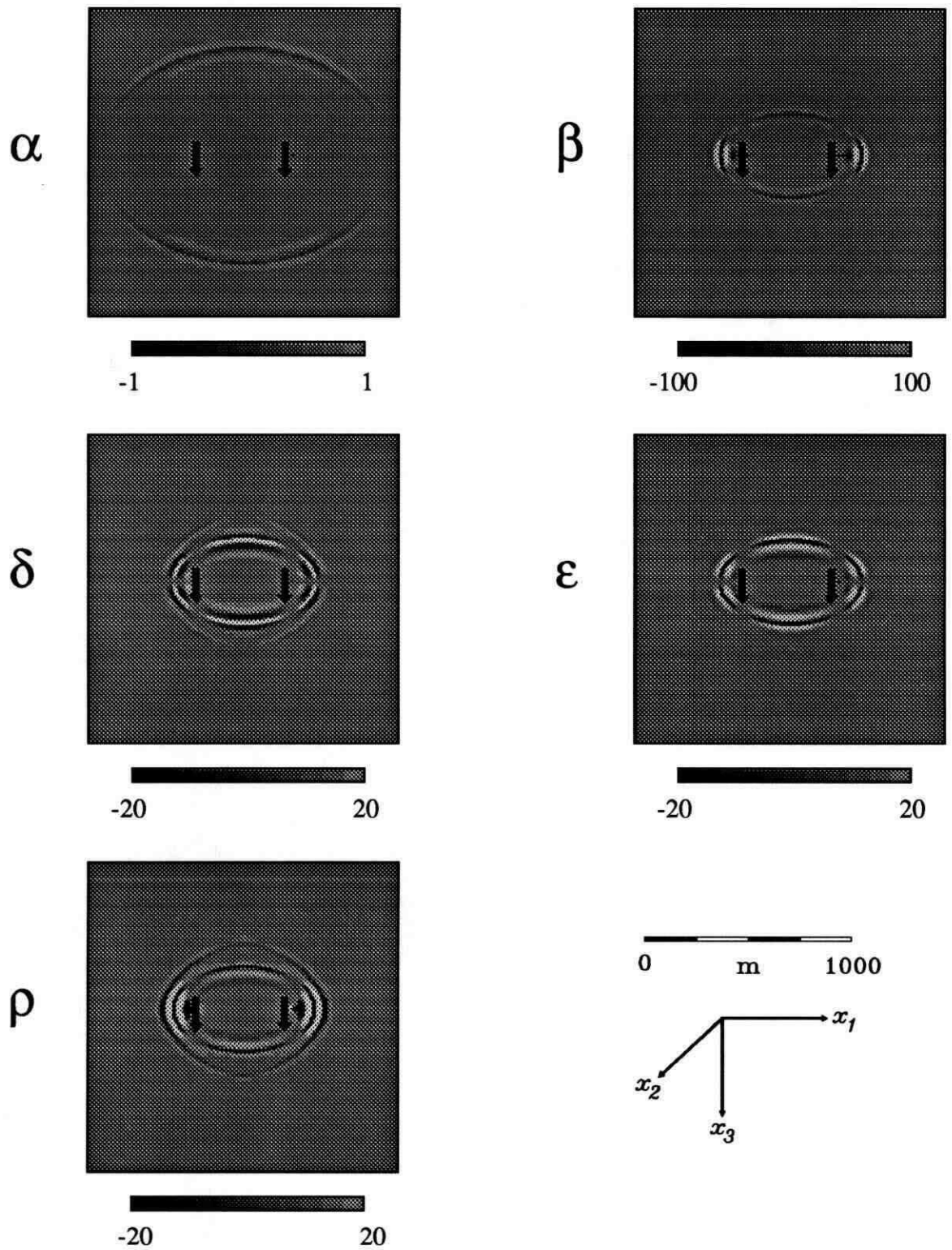
FIG. 11. Impulse response of filtered backprojection operator for vertical source (right-most arrow) and vertical receiver (leftmost arrow). Scale bars indicate plot amplitude.
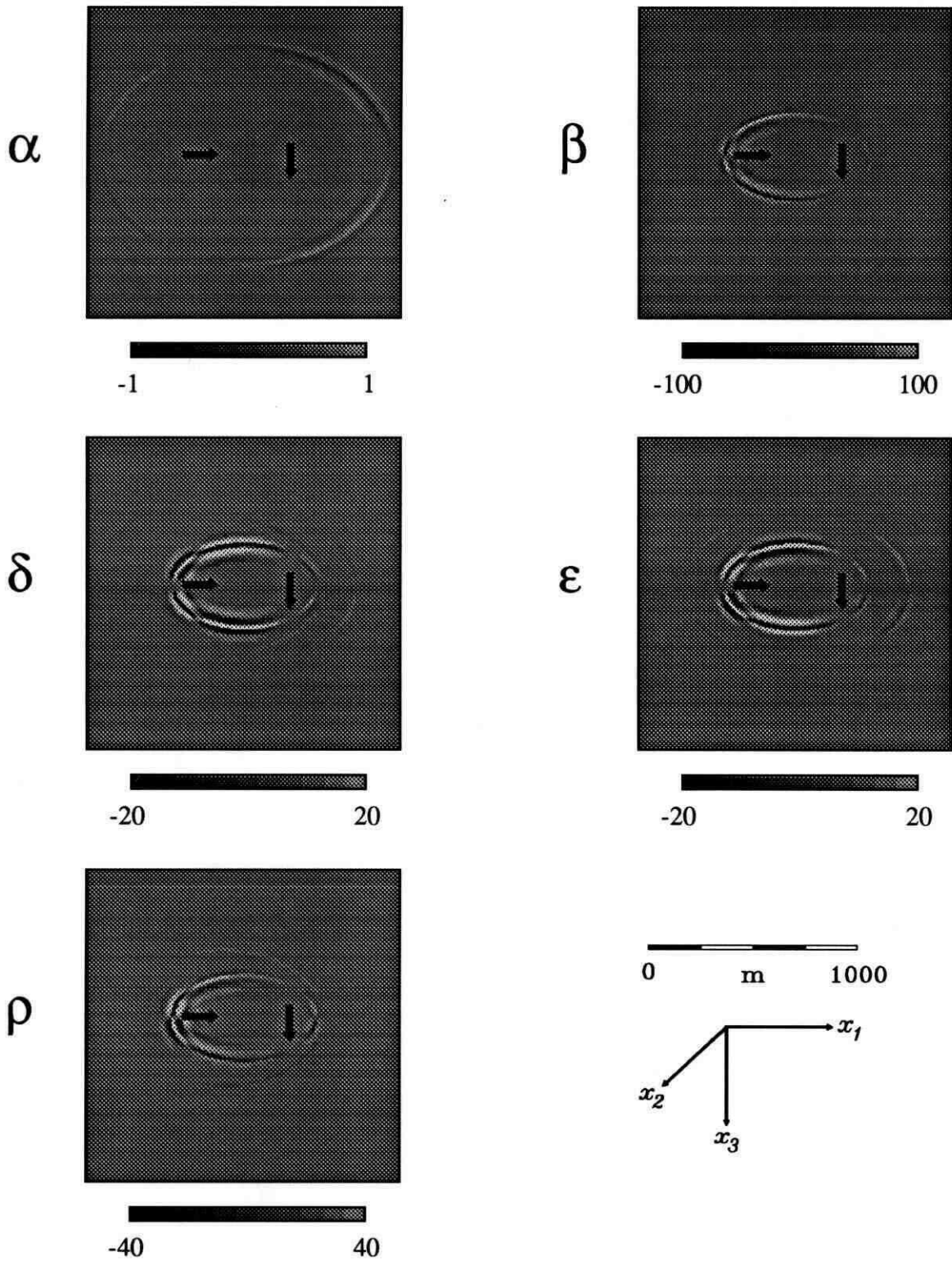
FIG. 12. Impulse response of the migration operator for a source (right-most arrow) and receiver (leftmost arrow) oriented as shown. Scale bars indicate plot amplitude.
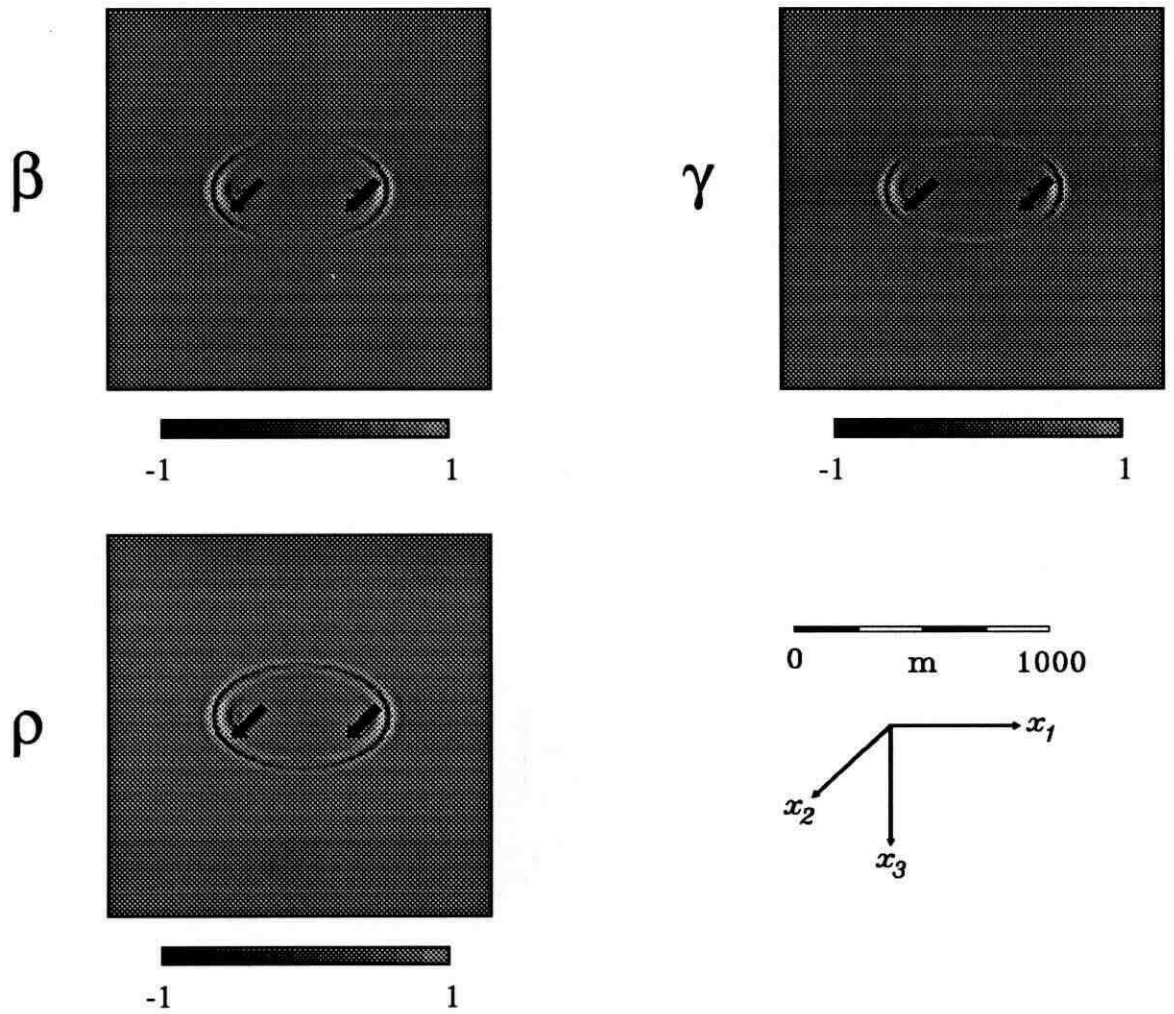
FIG. 13. Impulse response of the migration operator for source and receiver oriented in the x_2-direction.

these plots. The source and receiver are assumed to be located within an infinite, isotropic-homogeneous medium with parameters $\alpha = 3000$ m/s, $\beta = 1500$ m/s and $\rho = 2400$ kg/m^3. Note that, by including the source and receiver in the image zone, these examples violate the far-field assumption. In practice, a target zone would include only portions of the impulse response functions illustrated here.

Conventional Kirchhoff migration and acoustic ray-Born imaging techniques map individual data points to curves of constant traveltime in the model space (Schneider, 1978; Miller et al., 1988). Elastic migration/inversion is fundamentally different; data points are mapped to several iso-traveltime curves, cor-responding to the relevent subset from the set of ray codes { qP-qP, qP-qSV, qSV-qP, qSV-qSV, SH-SH }. For unconverted scattered events in a homogeneous-isotropic medium, these curves are elliptical, with foci at the source and receiver. The radius of curvature of the iso-traveltime path is the largest for qP-qP scattering, because of the generally higher velocity of qP-waves. For the same reason, iso-traveltime curves for converted events are normally shifted away from the source/geophone that is radiating/receiving qP waves.

Observe that the number of imaged parameters depends on the wave types radiated from the source, and received at the geophone. In Figure 13, where both the source and receiver are oriented in the x_2 (transverse) direction, only SH waves are scattered, and three of the six possible parameters are imaged (β,γ, and ρ). The other three plots involve P-SV scattering, and image five of the six parameters. The number of parameters imaged remains the same even in the presence of background aniso-tropy (although the impulse response can be much different), provided that the symmetry axis lies in the plane of acquisition. Hence, in order to resolve all six of the parameters, a complete nine-component (ie. 3-component sources and receivers) experiment is a practical requirement (otherwise sources and receivers would have to be oriented out of the plane such that all three wave types are radiated). However, it may be possible to invoke a statistical relationship between γ and ε (Eaton and Stewart, 1990), to reduce the number of parameters and thus avoid this complication.

MIGRATION/INVERSION EXAMPLES

We will consider four examples of the migration/inversion procedure applied to synthetic datasets. The acquistion geometry for the first two examples is illustrated in Figure 14. The first example consists of three end-on surface shot records of 12 traces each with a group interval and near offset of 50 m. The second example employs a crosswell acquisition geometry, with two sources at depths of 0 m and 2000 m, respectively, shooting into a set of 21 receivers in the second well, starting at the surface and each separated by 100 m. The background medium is the same as that used for the impulse-response plots, previously. The input data to the migration/ inversion algorithm was generated by scattering from seven points shown in Figure 14, using the ray-Born approximation (equation (15)). The central point represents a small positive perturbation to all six of the model parameters (α,β,γ,δ,ε,ρ). The other points represent small positive perturbations to individual parameters. Note that the axis of symmetry is taken to be vertical for these examples.
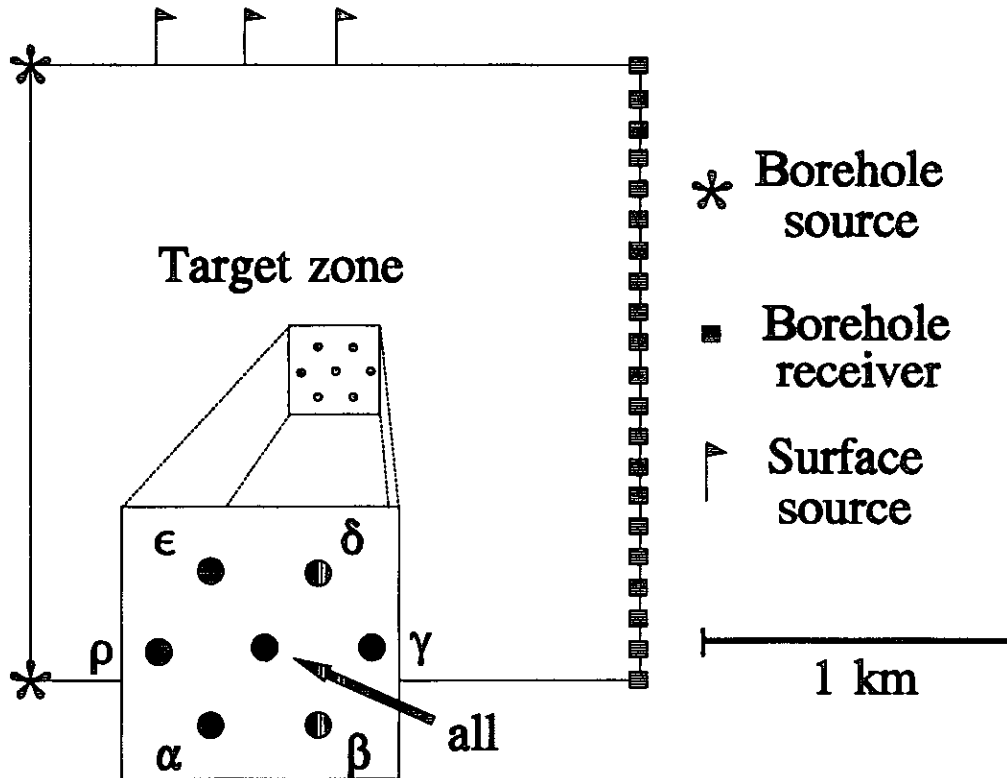
FIG. 14. Model geometry used for the first two examples. Example one consists of three surface shot records. Example two utilizes the crosswell shooting geometry. Inset shows the distribution and type of scattering points.

Figure 15a shows the scattered P-P and P-SV events calculated for this model. Note that these records have been modeled as pure-mode synthetics using a P-wave source. This simplification is realistic and valid in the presence of a low-velocity near-surface layer, which, coupled with the effect of the free surface, tends to effectively separate P and SV waves onto the vertical and radial recording channels, respectively (Eaton, 1988). The source wavelet is zero phase with a 5-15-55-90 Hz trapezoidal amplitude spectrum. These are the best possible data for the migration/inversion algorithm, since they satisfy all of the assumptions (far-field, single-scatter, etc.) and do not contain noise.

The M/I results for this input dataset are shown in Figure 16. The limited aperture of the recording geometry used for this example severely restricts the range of scattering angles. Artifacts that result from this restriction include smearing of the images, and parameter cross-coupling. Nevertheless, some of the essential features of the input model have been recovered, within the bandwidth of the source function. In particular, the isotropic parameters appear to be much better resolved than the
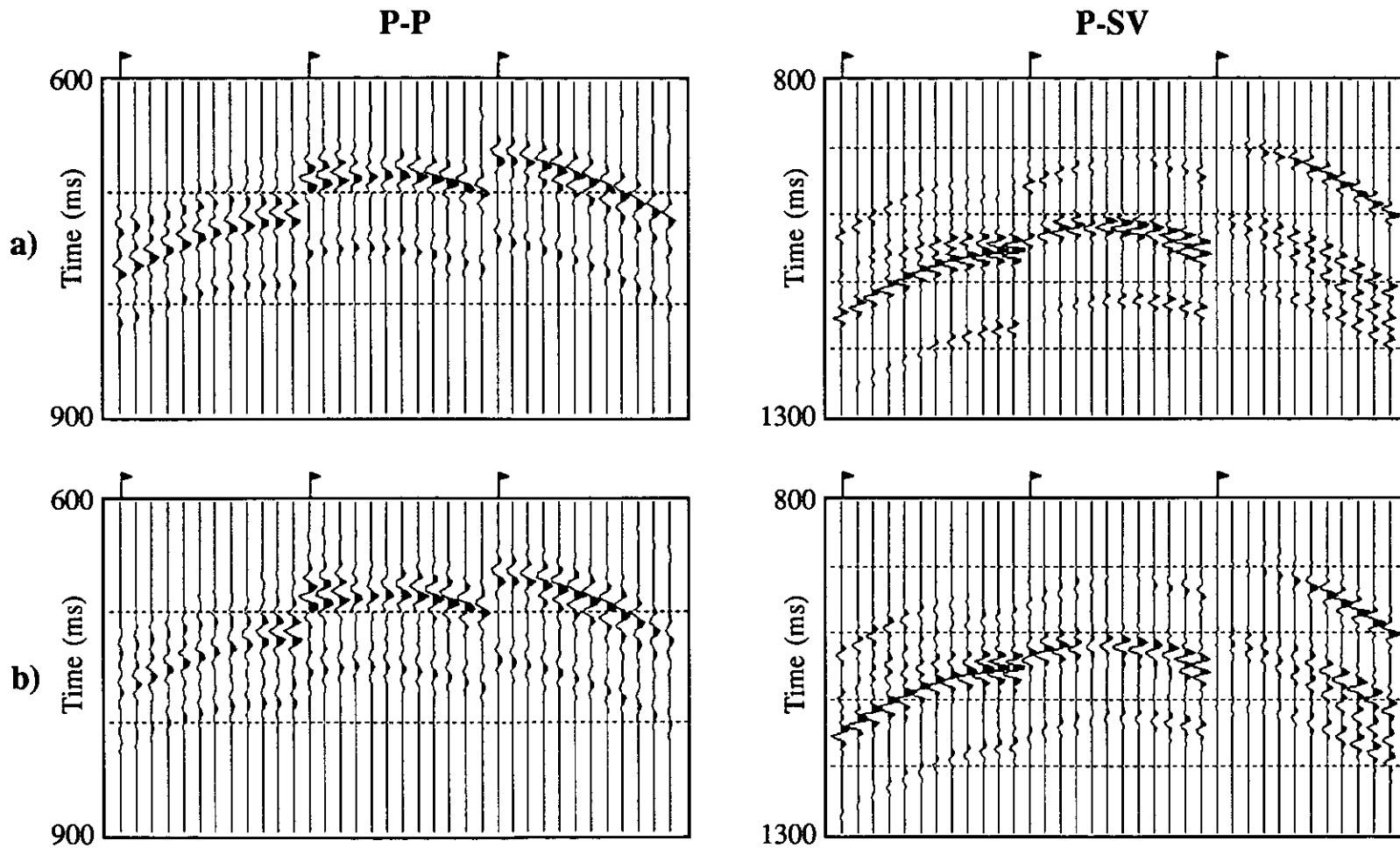
FIG. 15. a) Ray-Born synthetic data for model 1, used as input to the migration/inversion algorithm. Flags indicate the first trace for each shot record. b) Seismograms computed by scattering from the perturbation models shown in Figure 16.
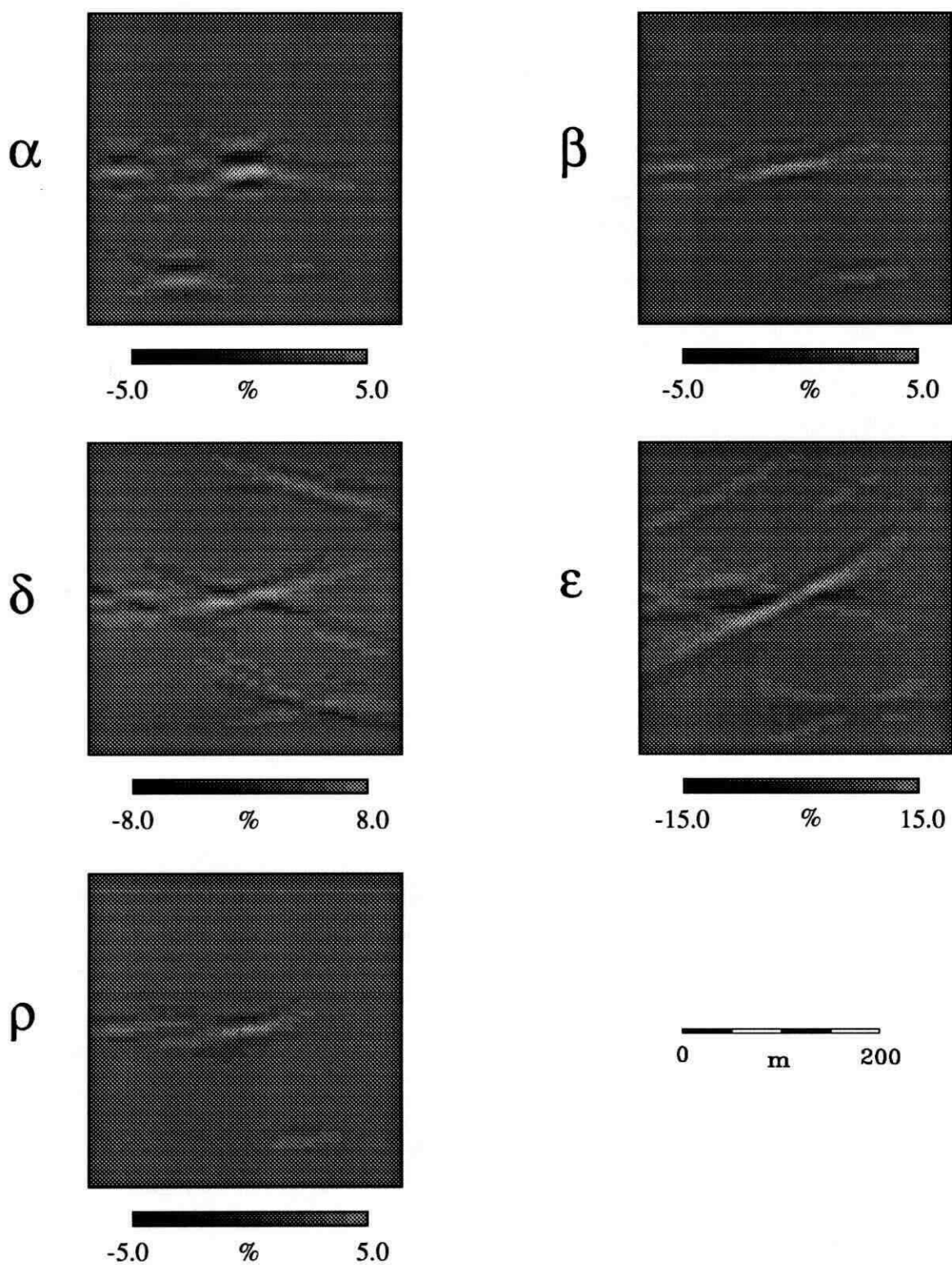
FIG. 16. Results of three iterations of migration/inversion for model 1. Scale bars show percent of actual perturbation magnitude used to generate the input data.

anisotropic parameters in this example. Some leakage of the ρ scattering point onto the α and β images suggests that perhaps P- and S-wave impedance would be a better parameterization for surface reflection data than α and β (Tarantola, 1986). No leakage of the anisotropic parameters onto the α, β and ρ images is apparent. Note that the anisotropic perturbations are not imaged as points, but as a criss-crossing linear feature.

Figure 15b shows seismograms computed by scattering from the perturbation models shown in Figure 16. The frequency content of the output traces is slightly lower than the frequency content of the input traces, due to the spatial smearing of the scattering points. The data residual, found by taking the difference between the traces in Figure 15a and 15b, is about 28% of the energy of the input traces. At first glance, the magnitude of the inversion results, expressed here as a percentage of the actual scattering strength, appears to be too small. However, in the Born approximation each point scatters energy independently. Thus, scattering from a collection of closely spaced, weak scatterers can produce results nearly identical to scattering from a single, large perturbation. Integrating the scattering response over a rectangular area of 40 m by 20 m, centred over the true position of the α perturbation, for example, gives a net scattering strength of 83% of the true perturbation. A summary of the integrated scattering strengths for this model over 40 m by 20 m rectangles appropriately positioned for each parameter is given in Table 1.

The calculated x_1-component traces for the crosswell example are shown in Figure 17a. In this case the source wavelet is zero phase with a 10-40-80-200 trapezoidal amplitude spectrum. The source is oriented in the x_1-direction, and radiates both P and SV waves. At each receiver position, both the x_1- and x_3-components of particle motion were modeled. The results after three iterations of migration/inversion are shown in Figure 18. Overall, the images of perturbations to α, β and ε are the most satisfactory. Arguably, the best inversion image for this example is ε, rather than any of the isotropic parameters. The magnitude of the inversion results was somewhat larger in this case (see Table 2), for reasons that are still uncertain. The re-scattered results are displayed in Figure 17b, for comparison with the input data. The residual energy in this case was only 8.5%. The algorithm seems to have the most difficulty matching the converted-wave response (middle panel in Figure 17).

The preceding examples have all featured a homogeneous background model. In practice it is unlikely that a homogeneous model will be sufficiently close to the

Parameter	α	β	δ	ε	ρ
Individual parameter	83 %	41 %	69 %	52 %	34 %
Centre of target zone	134 %	79 %	123 %	206 %	72 %

TABLE 1. Summary of integrated M/I perturbation values for the first example, for a rectangular area 40m × 20m in size.
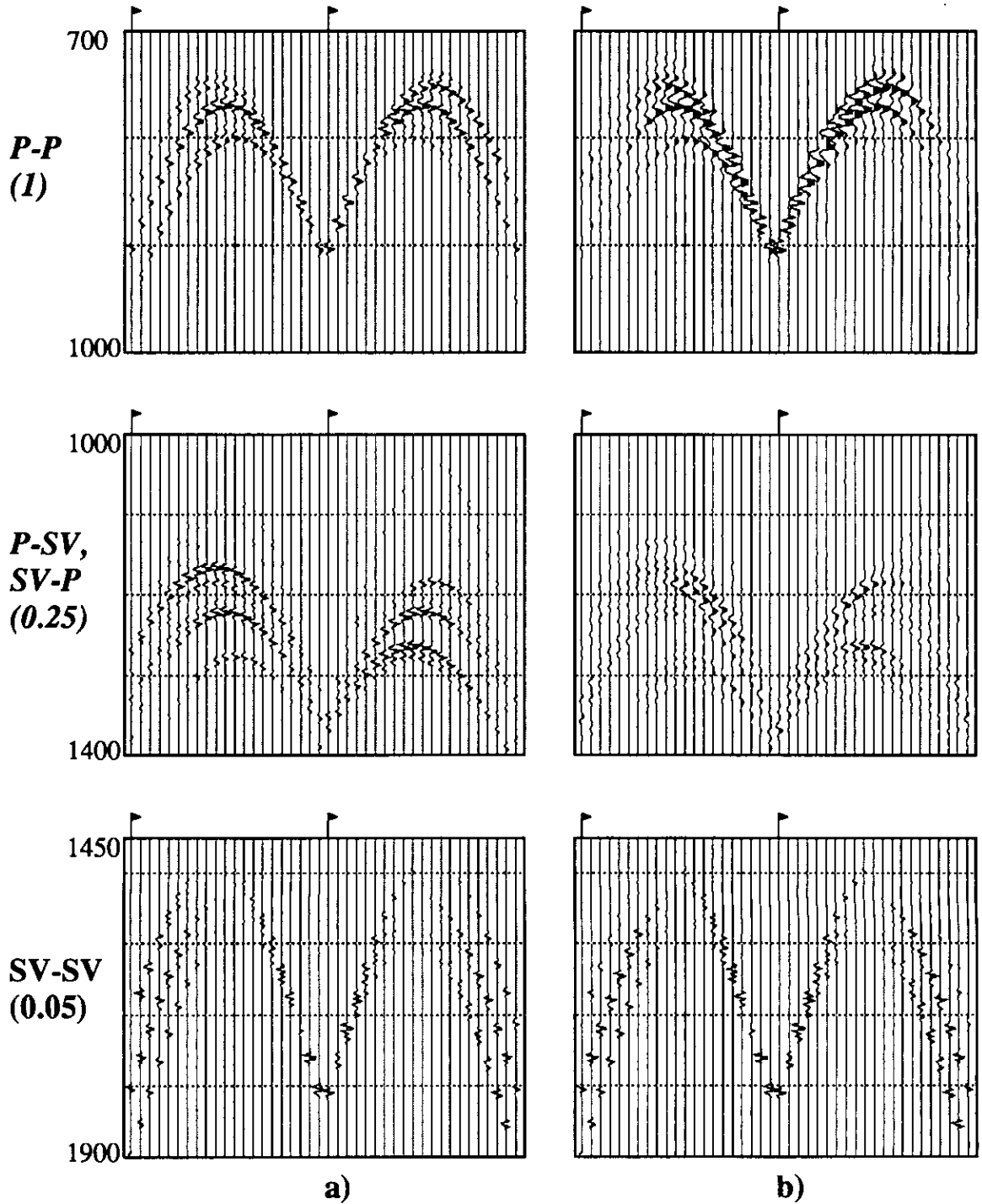
FIG. 17. a) Ray-Born synthetic data for model2, x_l-component. Flags indicate the first trace in a shot record. Time is in ms, and the number in brackets is the plot scalar used. b) Seismograms computed by scattering from the perturbation models shown in Figure 18.
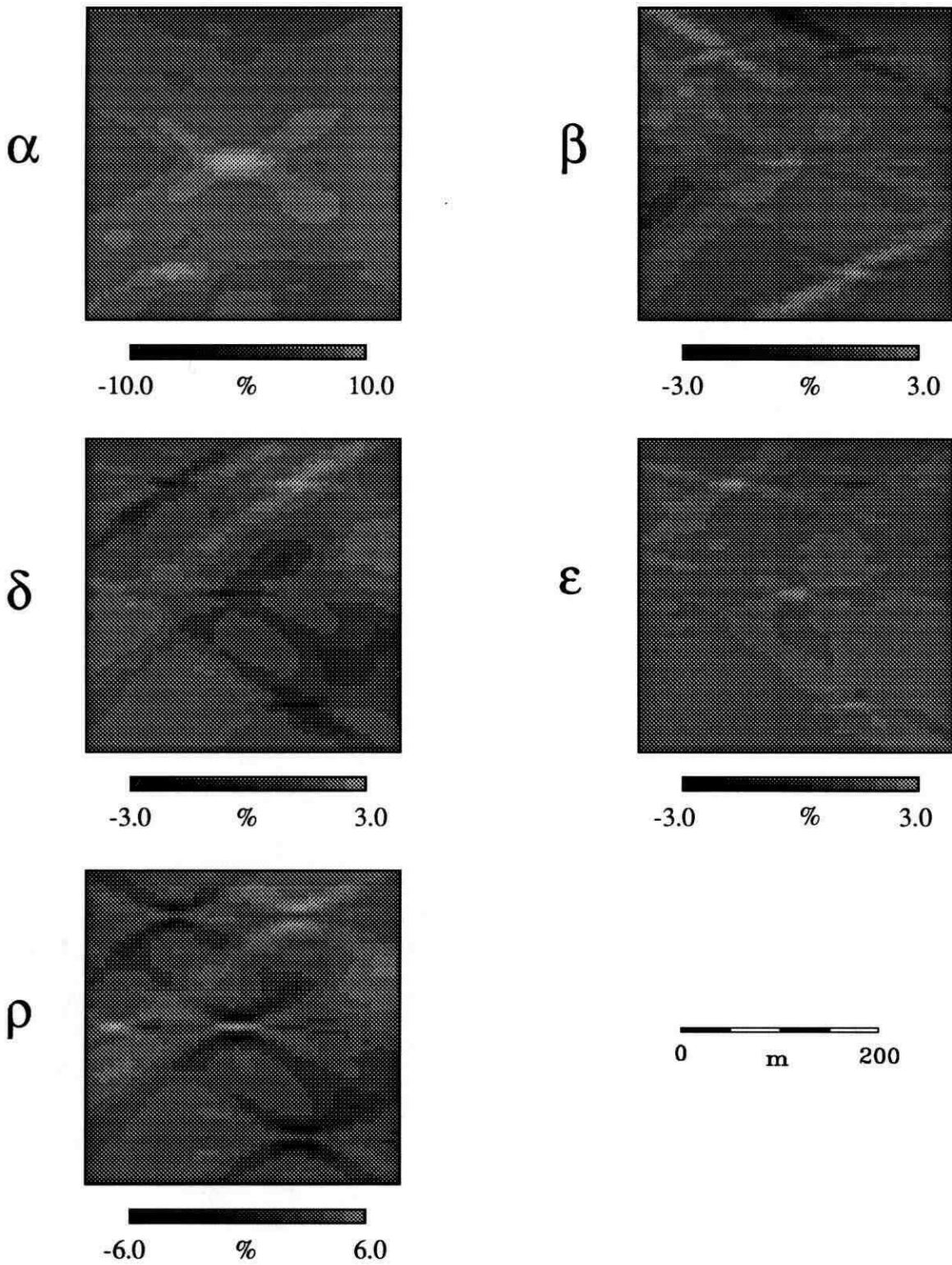
FIG. 18. Results of three iterations of migration/inversion for model 2. Scale bars indicate percent of acutal perturbation magnitude used to generate input data.

true earth to validate the Born approximation. The next example makes use of the anticline model discussed in the previous example concerning traveltime and amplitude calculation. A crosswell recording geometry was again used (Figure 5), consisting of 14 receivers at an interval of 50 m. However, there are no receivers within the transition layer because of severe amplitude anomalies associated with the strong heterogeneity in this zone. Three scattering points, each representing a small positive perturbation to α,β and ϵ, were used to generate the input ray-Born dataset (Figure 19). The target zone was not positioned around the fractured reservoir to avoid complications associated with the caustics near the zone.

Single-iteration M/I results for the third example are shown in Figure 20. Only isotropic perturbations were predicted by the M/I algorithm because, in this case, the *a priori* variance was chosen to be an extremely small number for the three anisotropic parameters, effectively damping their solution. The M/I results obtained here are very similar to isotropic migration results for synthetic data using a VSP geometry obtained by Beydoun et al. (1990). However, the background model used here is more complex and contains anisotropic layers.

A final example is used here to demonstrate the behaviour of the algorithm using a non-Born input dataset. The input data were generated using the Uniseis raytracing program, and are based on the reflection properties of plane waves at a smooth interface. The source wavelet is the same as in the previous crosswell examples. The background model is shown in Figure 21, and includes a sloping interface that becomes horizontal.

The x_l-component traces from the ray-traced input dataset (after removal of the direct arrivals) are shown in Figure 22. This dataset includes P-P, P-SV, SV-P and SV-SV reflections from the interface, but no diffractions. M/I results are shown in Figure 22. Unfortunately, parameter coupling effects as well as the non-Born nature of the modeled data have resulted in erroneous inversion results. For example, no change in δ,ϵ, or ρ exists at the interface, but these are all indicated in the inversion. However, the images do correctly show both the sloping and horizontal parts of the interface.

Note that because only P-P scattering is used in the inversion, the perturbation image for α has an appearance that is somewhat different from the other images. The same image, roughly speaking, would be produced by applying conventional depth migration techniques to the P-P reflection data. The different appearance is partially

Parameter	α	β	δ	ϵ	ρ
Individual parameter	185 %	60 %	57 %	26 %	67 %
Centre of target zone	316 %	46 %	54 %	36 %	163 %

TABLE 2. Summary of integrated M/I perturbation values for the second example, for a rectangular area 40m × 20m in size.
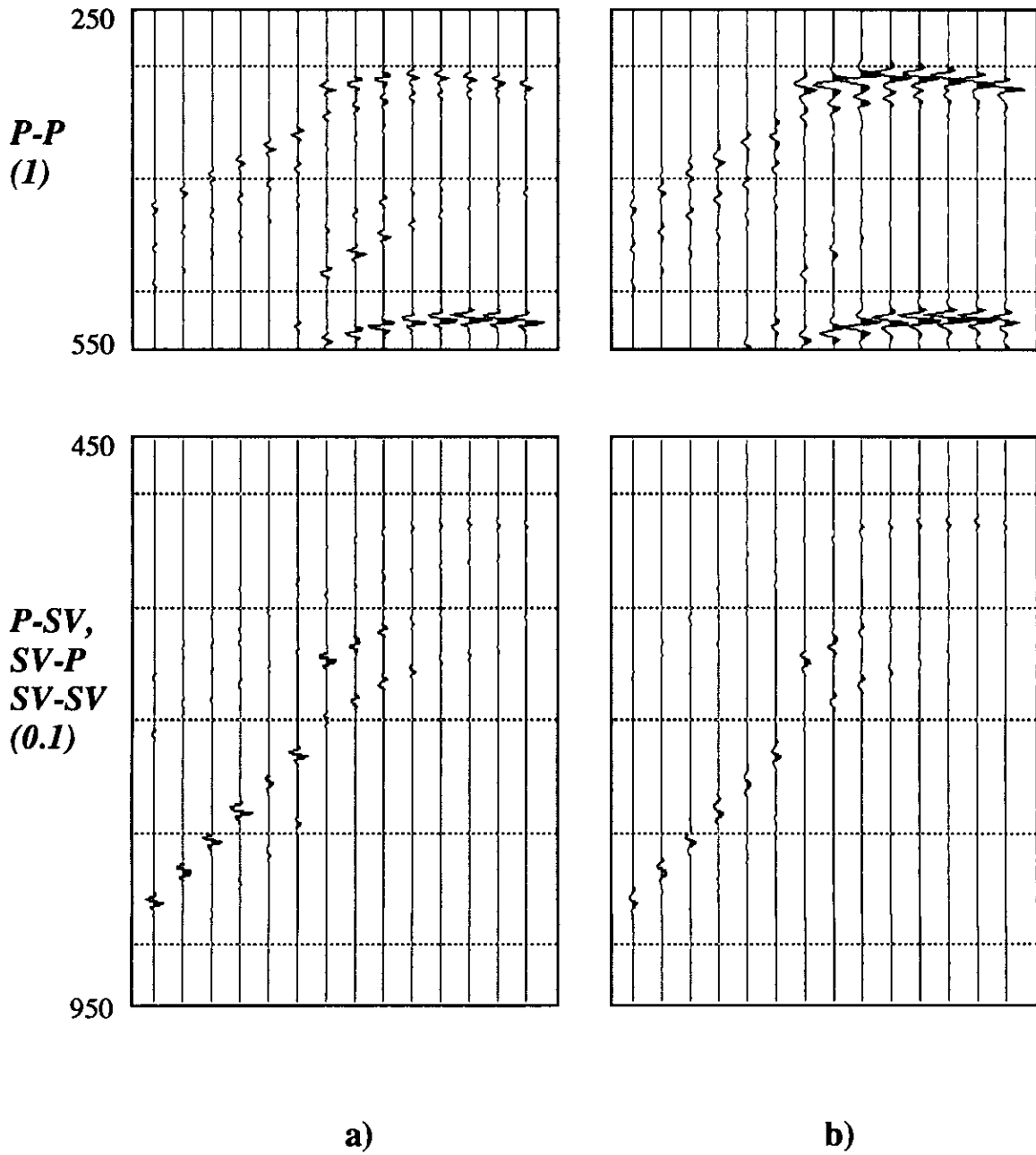
FIG. 19. a) Input data for model 4. Time is in ms, and number in brackets shows plot scalar used. b) Predicted data generated by scattering from migration/inversion results (Fig. 20).
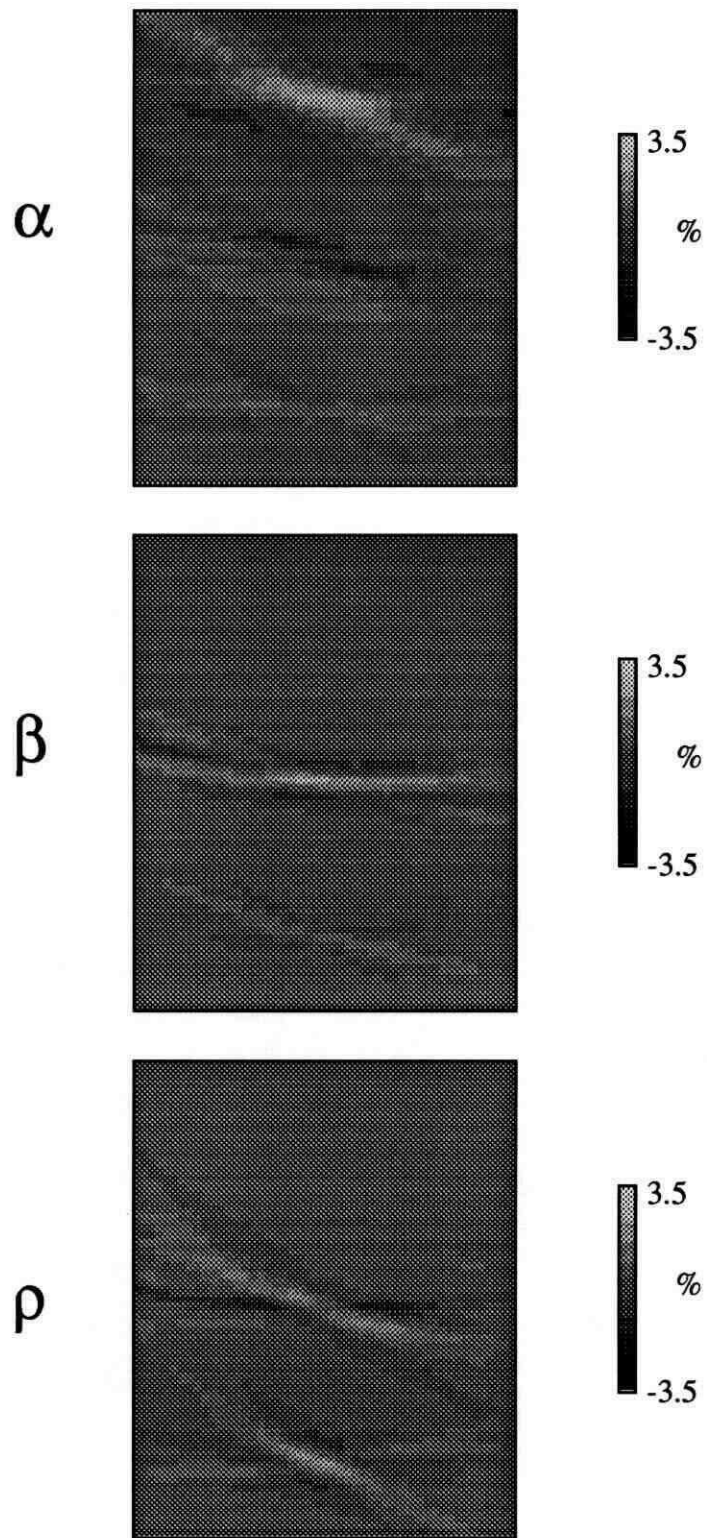
FIG. 20. Results of three iterations of migration/inversion for model 3.
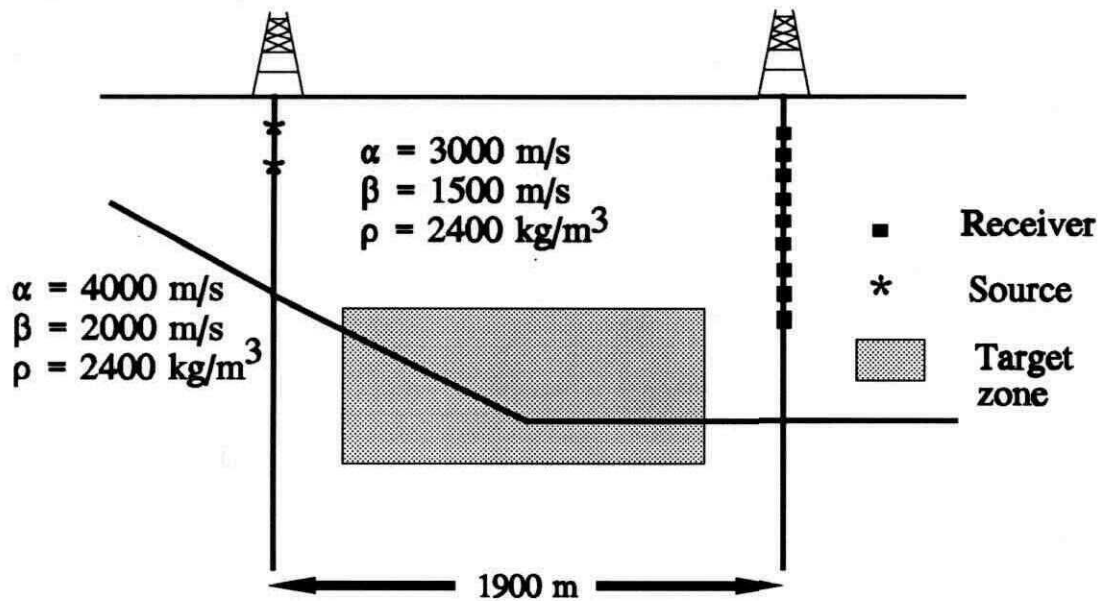
FIG. 21. Geological model and acquisition geometry used for example 4. Every second receiver position is shown.

due to the longer wavelength (and thus lower resolution) of *P*-waves than *SV*-waves, since the bandwidth of the source function is the same in both cases. More significant, however, is the fact that the segments of the interface illuminated by unconverted reflections are shorter than the segments illuminated when both unconverted and converted reflections are considered. Figure 24 illustrates this concept schematically, by showing the reflection raypaths connecting one of the sources to the first and last receivers. This result illustrates an important advantage of this migration/inversion approach, compared to conventional migration; by using all of the scattered wavetypes simultaneously, angular converage of the target zone is improved, thus giving improved resolution of geological features.

CONCLUSIONS

Several new techniques for seismic modeling and inversion, based on a transversely isotropic model for the earth, have been described briefly in this paper. First, a finite-difference methodology for computing ray-Green's functions has been developed, based on the work of Vidale (1988) and Vidale and Houston (1990) for calculating traveltimes and amplitudes in isotropic media. This approach has proven to be relatively fast, and is well suited to imaging applications because all of the quantities are available directly on a grid. However, the method works best for weakly
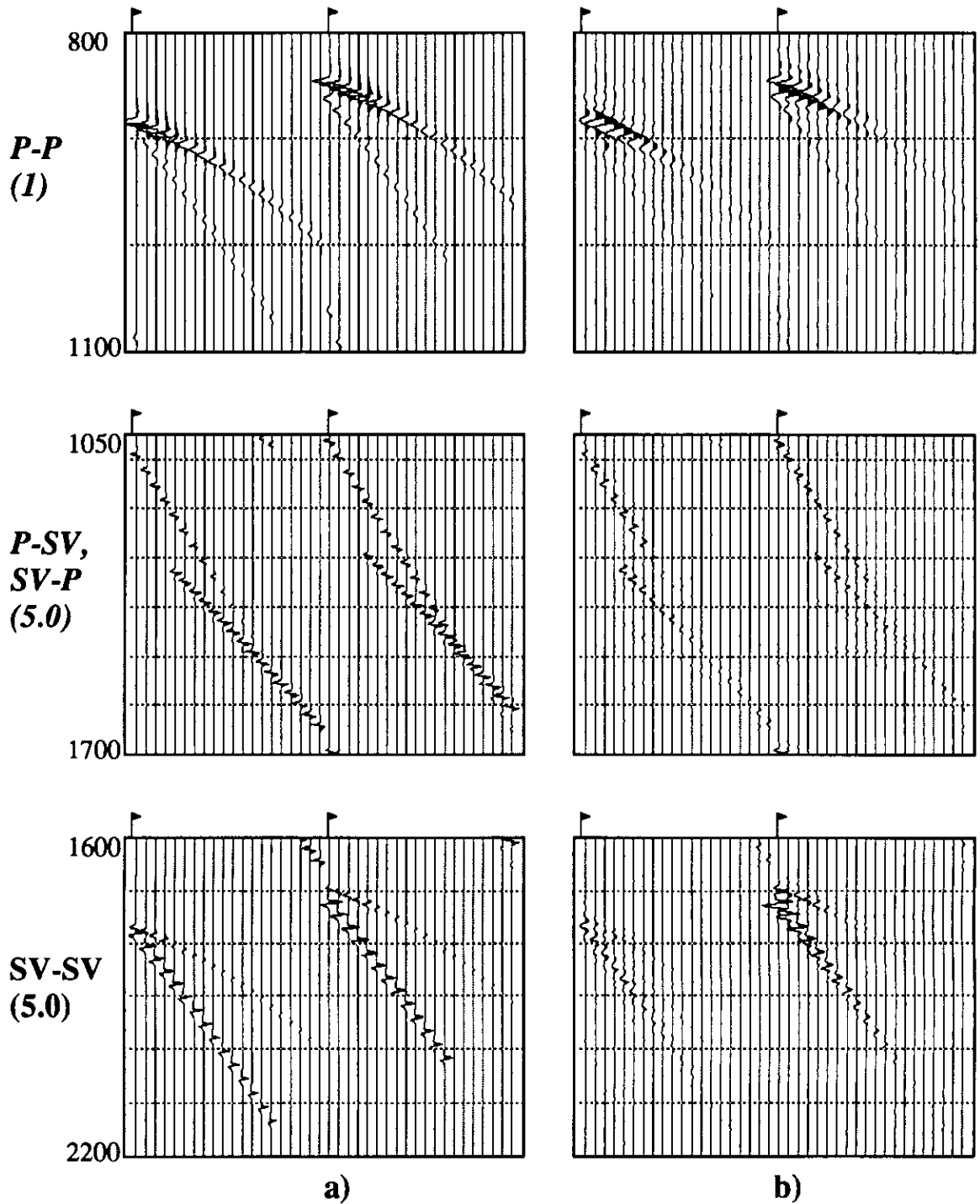
FIG. 22. a) Ray-traced input data for model 4. Flags indicate the first trace in a shot record. Time is in ms, and the number in brackets is the plot scalar used. b) Seismograms computed by scattering from the perturbation models shown in Fig. 23.
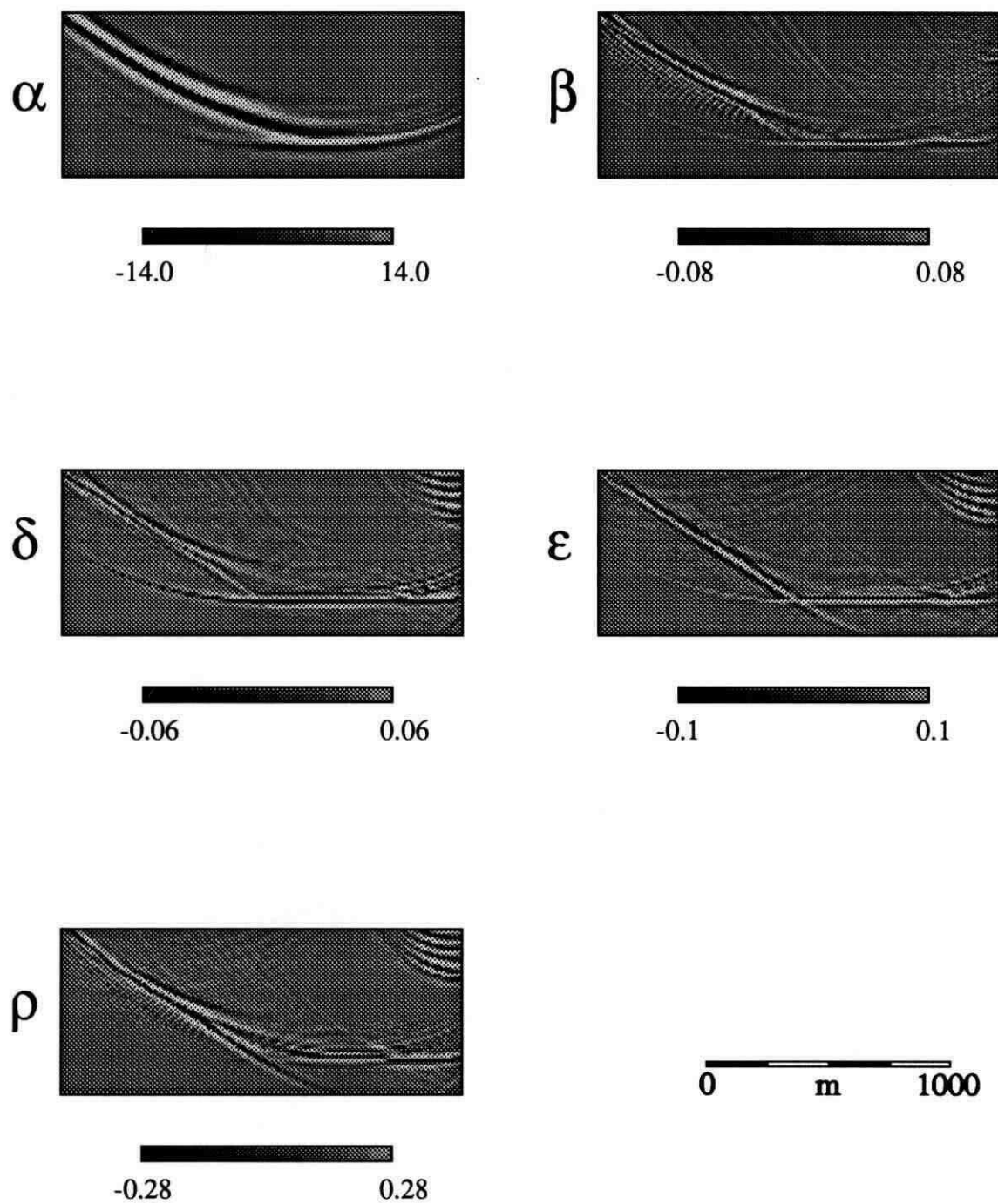
FIG. 23. Single-iteration migration/inversion results for model 5. Scale bars show relative magnitude for the inversion.

a)

Segment of interface
illuminated by
P-P reflections

b)

Segment of interface
illuminated by all
wave types
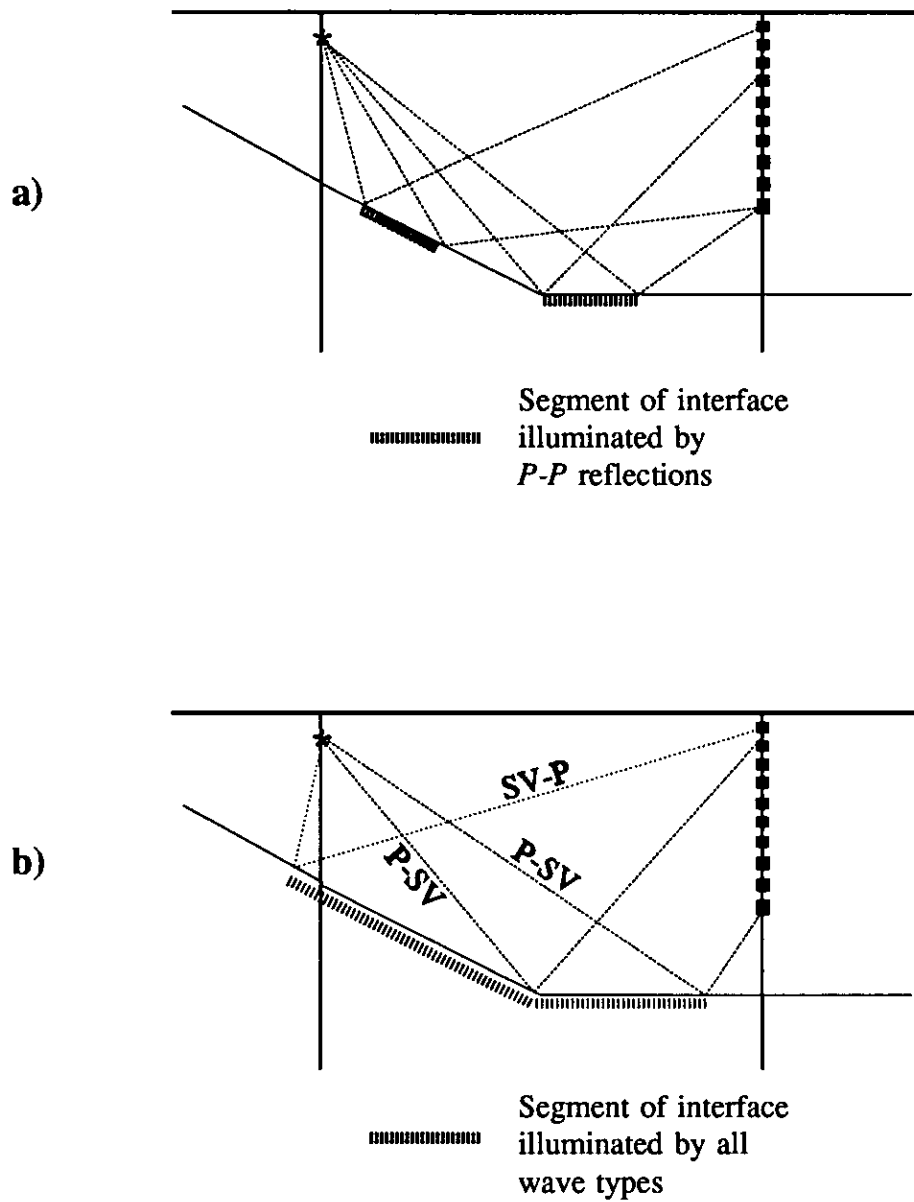
FIG. 24. Schematic illustration comparing the segments of the interface in model 4 illuminated by *P-P* reflection (a) with the segments illuminated by all of *P-P*, *P-SV*, *SV-P* and *SV-SV* reflections (b).

anisotropic media, for which problems associated with the qSV wavefront (eg. triplications, caustics and conical points) do not exist.

A previous elastic least-squares M/I scheme (Beydoun and Mendes, 1989) has been extended to include the case of transversely isotropic media with the axis of symmetry in the plane of acquisition. This methodology possesses certain inherent advantages over many other seismic imaging and inverson techniques. Unlike seismic migration, the close association between forward and inverse modeling can be exploited to permit some simple posterior analysis of the inversion results. Furthermore, this approach is intended to image intrinsic properties of a medium rather than its reflectivity, the latter depending also on the geometry and aperture of the acquisition experiment. The use of approximate ray-Green's tensors allows almost arbitrary configuration of the sources and receivers, as well as a very general form for the background model. The least-squares inversion method is flexible enough to accommodate prior information, in addition to insufficient and inaccurate observations. Finally, linearization of the problem guarantees that the Green's functions, governing propagation of the wavefield through the background medium, need to be computed only once. More general nonlinear techniques require very time consuming re-propagation of the wavefield for each iteration.

Testing of this algorithm using synthetic data has revealed that:
1) Under favourable conditions, anisotropic parameters (in particular, ε) can be recovered from crosswell seismic data. In some cases, resolution of ε appears to be better than any other parameter, isotropic or anisotropic.
2) These techniques are feasible, at least with small datasets, using present-day workstation technology.
3) Simultaneous migration of all available elastic wave types can improve seismic images and resolution of slope discontinuities in the subsurface.

REFERENCES

Adby, P.R., and Dempster, M.A.H., 1974, Introduction to optimization methods: Chapman and Hall.

Aki, K. and Richards, P.G., 1980, Quantitative seismology: W.H. Freeman and Company.

Beydoun, W.B., and Mendes, M., 1989, Elastic ray-Born l_2-migration/inversion: Geophys. J. Int., 97, 151-160.

Beydoun, W.B., Delvaux, J., Mendes, M., Noual, G., and Tarantola, A., 1989, Practical aspects of an elastic migration/inversion of crosshole data for reservoir characterizaton: A Paris basin example: Geophysics, 54, 1587-1595.

Beydoun, W.B., Mendes, M., Blanco, J., and Tarantola, A., 1990, North Sea reservoir description: Benefits of an elastic migration/inversion applied to multicomponent vertical seismic profile data: Geophysics, 55, 209-217.

Beylkin, G., 1985, Imaging of discontinuities in the inverse scattering problem by inversion of a causal generalized Radon transform: J. Math. Phys., 26, 99-108.

Beylkin, G., and Burridge, R., 1990, Linearized inverse scattering problems in acoustics and elasticity:

Wave Motion, **12**, 15-52.

Cerveny, V., 1972, Seismic rays and ray intensities in inhomogeneous anisotropic media: Geophys. J. Roy. Astr. Soc., **29**, 1-13.

Cerveny, V., Molotkov, I.A., and Psencik, I., 1977, Ray method in seismology: Univerzita Karlova, Prague.

Clayton, R.W., and Stolt, R.H., 1981: A Born-WKBJ inversion method for acoustic reflection data: Geophysics, 1559-1567.

Cohen, J.K., and Bleistein, N., 1979, Velocity inversion procedure for acoustic waves: Geophysics, **44**, 1077-1087.

Crampin, S., 1981, A review of wave motion in anisotropic and cracked elastic-media: Wave Motion, **3**, 343-391.

Crampin, S., Chesnokov, E.M. and Hipkin, R.A., 1984, Seismic anisotropy: The state of the art: Geophys. J. Roy. Astr. Soc., **76**, 1-16.

Duff, G.F.D., 1960, The Cauchy problem for elastic waves in an anisotropic medium: Phil. Trans. Roy. Soc. London, Ser. A: **252**, 249-273.

Eaton, D.W.S., 1989, The free surface effect: Implications for amplitude-versus-offset inversion: J. Can. Soc. Expl. Geophys., **25**, 97-103.

Eaton, D.W.S., 1990, Finite-difference solution of the eikonal equation for transversely isotropic media: CREWES Project Research Report, v. 2, 342-360.

Eaton, D.W.S., 1991, Seismic migration/inversion for transversely isotropic elastic media: Ph.D. thesis, The University of Calgary.

Eaton, D.W.S. and Stewart, R.R., 1990, 2-1/2 D elastic ray-Born migration/inversion theory for transversely isotropic media: CREWES Project Research Report, v. 2., 361-377.

Gajewski, D., and Psencik, T., 1987, Computation of high frequency seismic wavefields in 3-D laterally inhomogeneous anisotropic media: Geophys. J. Roy. Astr. Soc., **91**, 383-411.

Geoltrain, S., and Cohen, J.K., 1989, Asymptotic solutions to direct and inverse scattering in anisotropic elastic media: SEG 1989 Intl. Mtg., Expanded Abstracts, 938-942.

Kendall, J-M., and Thomson, C.J., 1989, A comment on the form of the geometrical spreading equations, with some numerical examples of seismic ray tracing in inhomogeneous, anisotropic media: Geophys. J. Int., **99**, 401-413.

Lebras, R., and Clayton, R.W., 1988, An iterative inversion of back-scattered acoustic waves: Geophysics, **53**, 501-508.

Levin, F.K., 1979, Seismic velocities in transversely isotropic media: Geophysics, **44**, 918-936.

Meadows, M., 1985, Exact and approximate inversion of plane-layered isotropic and anisotropic media by layer stripping: Soc. Expl. Geophys., 55th Ann. Int. Mtg., Expanded Abstracts, 336-339.

Milkereit, B., 1987, Migration of noisy seismic data: J. Geophys. Res., **92**, 7916-7930.

Miller, D., Oristaglio, M., and Beylkin, G., 1987, A new slant on seismic imaging: Migration and integral geometry: Geophysics, **52**, 943-964.

Musgrave, 1970, Crystal acoustics: Introduction to the study of elastic waves and vibrations in crystals: Holden-Day.

Qin, f., Olsen, K.B., Luo, Y., and Schuster, G.T., 1990, solution of the eikonal equaiton by a finite-difference method: Soc. of Expl. Geophys. Ann. Mtg., Expanded Abstracts, 1004-1007.

Raz, S., 1981, Direct reconstruction of velocity and density profiles from scattered field data: Geophysics, **46**, 832-836.

Rothman, D.H., 1988, Cellular-automaton fluids: A model for flow in porous media: Geophysics, **53**, 509-518.

Schneider, W.A., 1978, Integral formulation for migration in two and three dimensions: Geophysics, **43**, 49-76.

Stolt, R.H. and Benson, A.K., 1986, Seismic migration: Theory and practice: Geophysical Press.

Tarantola, A., 1986, A strategy for nonlinear inversion of seismic reflection data: Geophysics, **51**, 1893-1903.

Tarantola, A., 1987, Inverse problem theory: Methods of data fitting and model parameter estimation: Elsevier.

Thomsen, L., 1986, Weak elastic anisotropy: Geophysics, **51**, 1954-1966.

Tura, M.A.C., 1990, Acoustic and elastic diffraction tomography and its application to fracture detection, Ph.D. thesis, University of California at Berkeley, 182 pp.

Uren, N.F., Gardner, G.H.F., and McDonald, J.A., 1990, The migrator's equation for anisotropic media: Geophysics, **55**, 1429-1434.

Vidale, J.E., 1988, Finite-difference calculation of travel times: Bull. Seis. Soc. Am., **78**, 2062-2076.

Vidale, J.E., and Houston, H., 1990, Rapid calculation of seismic amplitudes: Geophysics, **55**, 1504-1507.

Weglein, A.B., Violette, P.B., and Keho, T.H., 1986, Using multiparameter Born theory to obtain certain exact multiparameter inversion goals: Geophysics, **51**, 1069-1074.

APPENDIX A

Referred to a co-ordinate system with the z-axis aligned with the anisotropic axis of symmetry, the stiffness matrix for a TI solid has the form

$$
\begin{bmatrix}
C_{11} & C_{12} & C_{13} & 0 & 0 & 0 \\
C_{12} & C_{11} & C_{13} & 0 & 0 & 0 \\
C_{13} & C_{13} & C_{33} & 0 & 0 & 0 \\
0 & 0 & 0 & C_{44} & 0 & 0 \\
0 & 0 & 0 & 0 & C_{44} & 0 \\
0 & 0 & 0 & 0 & 0 & C_{66}
\end{bmatrix} , \qquad \text{(A-1)}
$$

where $C_{12} = C_{11} - 2C_{66}$. Substituting (A-1) into the eikonal equation (1) and solving for p_3 leads to a sixth-order polynomial,

$$
\xi_j p_3^{\,j} = 0 \quad , \quad j=0,...,6 \quad . \qquad \text{(A-2)}
$$

Defining

$$
A_{ik} \equiv c_{i3k3}
$$

$$
B_{ik} \equiv (c_{i3kl} + c_{ilk3})p_1 \quad , \qquad \text{(A-3)}
$$

$$
C_{ik} \equiv c_{ilkl}p_1^2 - \rho\delta_{ik}
$$

the coefficients of this polynomial may be written

$$
\xi_0 = |A|
$$

$$
\xi_1 = |AAB| + |ABA| + |BAA|
$$

$$
\xi_2 = |AAC| + |ACA| + |CAA| + |ABB| + |BAB| + |BBA|
$$

$$
\xi_3 = |ABC| + |ACB| + |BAC| + |BCA| + |CAB| + |CBA| + |B| \quad , \qquad \text{(A-4)}
$$

$$
\xi_4 = |ACC| + |CAC| + |CCA| + |BBC| + |BCB| + |CBB|
$$

$$
\xi_5 = |BCC| + |CBC| + |CCB|
$$

and

$$
\xi_6 = |C| \quad .
$$

In equation (A-4), the notation $[ABC]$ is used to represent a matrix whose first row comes from A, the second from B and the third from C. Thus, the coefficients of the

polynomial equation are found using the determinants of matrices that are row-permutations of the matrices defined in (A-3).

APPENDIX B

In equation (15), the matrix **L** transforms the model perturbation vector from units of $(\alpha, \beta, \gamma, \delta, \varepsilon, \rho)$ to elastic stiffnesses. For this model parameterization,

$$\mathbf{L} = \begin{bmatrix} 2\rho\alpha(2\varepsilon+1) & 0 & 0 & 0 & 2\rho\alpha^2 & \alpha^2(2\varepsilon+1) \\ 2\rho\alpha & 0 & 0 & 0 & 0 & \alpha^2 \\ \zeta_1 & \zeta_2 & 0 & \xi 2\rho^2\alpha^2(\alpha^2-\beta^2) & 0 & \zeta_3 \\ 0 & 2\rho\beta & 0 & 0 & 0 & \beta^2 \\ 0 & 2\rho\beta(2\gamma+1) & 2\rho\beta^2 & 0 & 0 & \beta^2(2\gamma+1) \\ 0 & 0 & 0 & 0 & 0 & 1 \end{bmatrix} \tag{B-1}$$

where:

$$\zeta_1 = \xi(8\rho^2\alpha^3\delta - 4\rho^2\beta^2\alpha\delta + 4\rho^2\alpha(\alpha^2-\beta^2)) \quad ;$$

$$\zeta_2 = -\xi(4\rho^2\alpha^2\beta\delta + 4\rho^2\beta(\alpha^2-\beta^2)) \quad ;$$

$$\zeta_3 = \xi[4\rho\alpha^2\delta(\alpha^2-\beta^2) + 2\rho(\alpha^2-\beta^2)] - \beta^2 \quad ;$$

$$\xi = [2\rho^2\alpha^2(\alpha^2-\beta^2)\delta + \rho^2(\alpha^2-\beta^2)^2]^{1/2} \quad .$$

$$\tag{B-2}$$

The parameters in (B-1) and (B-2) refer to the background medium; hence, for an isotropic background, γ, ε and δ are all zero.